Cation exchange modification of clinoptilolite – Screening analysis for potential equilibrium and kinetic adsorption separations involving methane, nitrogen, and carbon dioxide

D.A. Kennedy, F.H. Tezel*

Department of Chemical and Biological Engineering, University of Ottawa 161 Louis Pasteur, CBY A412, Ottawa, K1N 6N5, ON, Canada

A B S T R A C T

In this study, natural clinoptilolite was modified by cation exchange using alkali metal cations (Li^+, Na^+, K^+, Rb^+, Cs^+), alkaline earth metal cations (Be^{2+}, Mg^{2+}, Ca^{2+}, Sr^{2+}, Ba^{2+}), transition metal cations (Fe^{3+}, Ni^{2+}, Cu^{2+}, Zn^{2+}, Ce^{3+}), and acid treatment (H^+). The composition and structural properties of the modified samples were assessed using EDS and XRD analysis, and compared to the original clinoptilolite sample. Adsorption isotherms for CO_2, N_2, and CH_4 gases were measured using a microgravimetric adsorption analyser. For all of the clinoptilolite samples, the adsorption equilibria and the diffusion rates were measured at 303 K over a pressure range from 0 to 8atm. The results of this screening analysis show that the cation exchanged clinoptilolites exhibit a wide range of adsorption characteristics, which make them suitable for a variety of gas separation applications by pressure swing adsorption. The high adsorption selectivity towards CO_2 and CH_4 found with the Cs^+ exchanged clinoptilolite makes it advantageous for possible CH_4/N_2 and CO_2/N_2 equilibrium separations. Reduced CH_4 equilibrium capacity resulting from pore blocking in the Ca^{2+} exchanged clinoptilolite leads to high selectivity for CO_2/CH_4 and N_2/CH_4 selective adsorbent. However, the potential of this material is limited due to increased microporous diffusion resistance. While both Li^+ and Ni^{2+} clinoptilolites exhibit low CH_4/N_2 ideal selectivity, they present high N_2/CH_4 kinetic selectivity, thereby making them suitable for possible N_2/CH_4 kinetic separations.

1. Introduction

The development and application of new or modified small pored adsorbent materials for gas separations using adsorption technology is of interest for a broad range of industrial separations. The separation of carbon dioxide, methane, and nitrogen containing mixtures are of particular importance due to potential economic and environmental implications. Specifically, the capture of CO_2 from industrial flue gases containing N_2, as well as the separation of CO_2 and N_2 from CH_4 in applications of enhanced natural gas and coal bed gas recovery, biogas production, and control of fugitive methane emissions have been important areas of research. The potential application of pressure swing adsorption (PSA) technology for these separations may be accomplished through exploiting differences in adsorption equilibrium and kinetic properties of the gases with the adsorbents.

Adsorption separations are governed by equilibrium and kinetic effects [1]. Due to differences in their molecular properties as shown in Table 1, the equilibrium adsorption potential of the gases in the order of increasing capacity is: $N_2 < CH_4 < CO_2$, in general. The electrostatic

surface potential is the highest for CO_2 as it has a combination of high polarizability and strong quadrupole moment which favours its adsorption over both CH_4 and N_2. Due to its low polarizability and a weak quadrupole moment compared to the other two gases, N_2 generally has the lowest adsorption potential compared to both CO_2 and CH_4.

For the implementation of an economical PSA process for biogas or natural gas recovery, it is ideal to employ a PSA cycle in such a way that the desired component (CH_4) remains in the high pressure raffinate stream. This is to limit the requirement for recompression of the product gas following the gas separation step. For this to be achieved, the adsorption of CH_4 should be limited in such a way that the affinity towards the adsorbent follows the trend of $CH_4 < N_2 < CO_2$. The desired properties may be achieved in such a way that adsorption of the larger CH_4 gas molecule is inhibited thus inducing a favourable separation towards the smaller gases. However, separation of these gases through kinetic and molecular sieving is difficult, since their kinetic diameters are very similar.
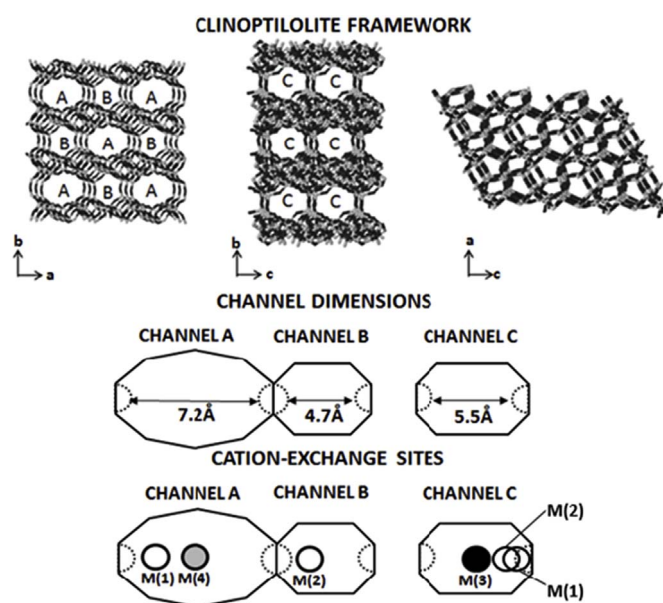
For the application of these gas separations using adsorption, the idea of porous solids with discrete and uniform micropores ranging in

---

Table 1
Relevant molecular properties of CO_2, CH_4, and N_2 gases [2,3].

gas	Molecular weight (g·mol^{-1})	kinematic diameter (Å)	polarizability ($\times 10^{-25}$ cm^3)	dipole moment ($\times 10^{18}$ esu·cm)	quadrupole moment ($\times 10^{-26}$ esu·cm^2)
CO_2	44	3.30	29.1	0	4.30
CH_4	14	3.82	26.0	0	0
N_2	28	3.64	17.4	0	1.52

Fig. 1. The framework structure of clinoptilolite zeolite as described by the International Zeolite Association with the channel dimensions and approximated M(1) through M(4) exchangeable cation positions for the naturally occurring cations [44,45].

size between 3 Å and 4 Å coupled with high pore volume are of interest. Typical areas of research for separation of N_2 from CH_4 containing mixtures have focussed on the development small pored adsorbents, such as ordered microporous carbon molecular sieves (CMS) [4], tita-nosilicates (ETS-4) [5–7], small pored LTA structured zeolites (4A) [8], and cation exchanged clinoptilolite zeolites [9–12]. Additionally, many contributions exist regarding CO_2 removal from CH_4 and N_2 containing mixtures using various materials, including: LTA type zeolites [13,14], MFI type zeolites [15–19], activated carbons [20,21], chabazites [22], among many others [23,24].

Microporous carbon molecular sieves have been investigated for possible kinetic separations of CO_2 and N_2 from CH_4 mixtures for nat-ural gas or landfill gas upgrading [25–27]. Although CMS has higher equilibrium capacity for CH_4 compared to N_2, it is kinetically selective for N_2 due to its narrow pore size distribution and small micropore size. This leads to a delay in the adsorption uptake of CH_4 over N_2 since it is more difficult for the larger CH_4 to access the pores of the adsorbent. Cavenati et al. proposed a layered PSA system containing CMS and 13X zeolite layered in a packed bed which was capable of producing 92% pure methane with 43.5% recovery from a mixed CO_2-CH_4-N_2 gas feed [28]. Similarly, small pored LTA structured zeolites such as zeolite 4A has been proposed for a possible kinetic separation of N_2 from CH_4. However, the proposed PSA process is limited to low temperatures (below 277 K) and CH_4 feeds of greater than 90%. With respect to N_2/CH_4 selective adsorbents using adsorption equilibria as a means of se-paration, titanosilicate ETS-4 has been proven to be tailored as a N_2 selective molecular sieve through activation at temperatures between 270 °C and 315 °C resulting in a contracted pore size [5]. ETS-4 has some industrial success for methane recovery under the commercial name Molecular Gate Adsorption Technology®. While substantial N_2/

CH_4 equilibrium selectivity has been reported, an ongoing limitation of this adsorbent is the relatively low capacity for N_2 gas with a reported equilibrium saturation N_2 adsorption capacity of between 0.5 and 0.6 mmol/g at ambient temperatures [5–7]. MIL-100(Cr) which is a metal organic framework (MOF) material has shown promise for N_2/CH_4 equilibrium selective separations, however issues remain with re-spect to the stability of MOF type materials for long term PSA type applications [29]. Additionally changes in the cation composition of modified zeolite rho has shown to effect the pore size of this zeolite, thus inducing favourable adsorption and molecular sieving properties for CO_2, CH_4, and N_2 separations [30].

Clinoptilolite is an abundant naturally occurring microporous zeo-lite with a two dimensional channel structure that is isostructural to the heulandite (HEU) group of zeolites [31]. As described by Ackley and Yang [9,11], clinoptilolite is composed of a framework of alternating 10 and 8-membered rings which form two parallel channels (channels A and B respectively) that intersect with a third channel composed of an 8-membered ring (channel C). The approximate dimensions of the channels are as follows: channel A = 7.2 Å × 4.4 Å, channel B = 4.7 Å × 4.1 Å, and channel C = 5.5 Å × 4.0 Å. The framework of clinoptilolite is composed of SiO_4 and AlO_4^{-1} tetrahedra with typical Si/Al ratios for natural clinoptilolite ranging from 4 to 5.2 [32]. This results in an unbalanced negative framework with charge balancing cations occupying sites within the channel pore network of clin-optilolite, where Na^+, K^+, Ca^{2+}, and Mg^{2+} are the most common naturally occurring charge balancing cations.

The crystal structure and cation organization of clinoptilolite is very interesting due to the existence of multiple extra framework cation sites and high cation exchange capability. Previous work completed by Koyama and Takeuchi established the existence of 4 extra framework cation sites denoted M(1) through M(4) [33]. These locations corre-spond to the locations of the naturally occurring cations present in HEU type zeolites: Na^+, Ca^{2+}, K^+, and Mg^{2+}, respectively. Since this early work, extensive crystallographic studies on the location of other cations in HEU type zeolites have proved the cation exchange ability and identified several different extra framework locations for samples ex-changed with cations including: Ag^+, Pb^{2+}, Cd^{2+}, Mn^{2+}, Hg^{2+}, Ba^{2+}, Rb^+, Cs^+, Zn^{2+}, Cu^{2+}, Co^{2+}, Ni^{2+} and NH_4^+ [34–43]. Fig. 1 presents the framework structure of clinoptilolite and the approximated extra framework cation locations M(1) through M(4) for the naturally oc-curring cations.

The M(1) through M(4) extra framework cation sites are the most well understood positions. The distribution of the cation exchange lo-cations are variable and depend on the cation size and charge, and may also be coordinated with the zeolite framework and/or water molecules [33,43,46,47]. For example, variable cation coordination and migration has been demonstrated with Zn^{2+}, K^+, and Na^+ exchanged clin-optilolite and heulandite type zeolites at higher temperatures as a result of framework dehydration [41,46,48]. Godelitsas and Armbruster have demonstrated that the positions of several cations are also influenced by the positioning of water molecules present within the channels of the zeolite [42].

The distribution and location of the major exchangeable cation sites residing within the channels of clinoptilolite influences the overall adsorption equilibrium and the diffusion characteristics of gases within the zeolite [9,11,49]. Within the channel network, the M(1) and M(2)

Table 2
Preferred positions for the naturally occurring extra-framework cations present in clinoptilolite [44].

Cation Exchange Position	Channel	Channel Dimension (Å × Å)	Known Exchangeable Cations
M(1)	A	7.2 × 4.4	$Na^+ > Ca^{2+}$
M(2)	B	4.7 × 4.1	$Ca^{2+} < Na^+$
M(3)	C	5.5 × 4.0	K^+
M(4)	A	7.2 × 4.4	Mg^{2+}

sites have been reported to be preferred to be occupied by Na^+ and Ca^{2+} cations, respectively, whereas the M(3) site has been shown to be preferred by K^+, and the M(4) site is preferred by Mg^{2+} and Li^{2+} respectively. It has been speculated by Jayaraman et al. based on pure CH_4 and N_2 adsorption data that Ce^{3+} cations may prefer to occupy the M(4) and M(3) sites [50]. Table 2 shows a summary of the location of the naturally occurring exchangeable cations given in the literature limited to M(1) through M(4) sites for simplicity [45]. Due to the proximity of some of the cation exchange sites, only some of the sites may be occupied simultaneously in pair combinations, with the adjacent M(1)-M(3) and M(1)-M(4) site combinations not always possible because of steric hindrance due to restrictions of the atomic size and positions within the sites.

Clinoptilolite has been shown to exhibit interesting adsorption equilibria and diffusion behaviour due to its unique channel geometry and cation exchange capability. This variable kinetic and equilibrium gas separation capability is derived from the two dimensional pore structure and the pore blocking effects of the highly exchangeable extra framework cations within the channels [44]. Frankiewicz and Donnelly observed that the presence of partially exchanged divalent Ca^{2+} cations in naturally occurring clinoptilolite results in a N_2/CH_4 kinetic and equilibrium selective adsorbent, however further study into the use of this adsorbent in a PSA process resulted in a product that was below pipeline quality [51]. Ackley and Yang characterised the pure component equilibrium adsorption, diffusion uptake, and isosteric heat of adsorption data of N_2 and CH_4 on clinoptilolites exchanged with Na^+, K^+, H^+, Mg^{2+}, and Ca^{2+} [11,12,44]. They found that N_2/CH_4 selective equilibrium adsorption was achieved with clinoptilolites modified with Na^+ and partially modified (89%) with Ca^{+2} cations. These cations occupy the M(1)-M(2) extra-framework sites, effectively blocking CH_4 from accessing channels B and C respectively. The Mg^{+2} cations occupying the M(4) position were not exchanged, and were suspected to block channel A in the partially exchanged samples [11,12]. Chromatographic studies by Triebe and Tezel confirmed that microporous diffusion of N_2 and CO is dominant in natural clinoptilolite [52]. Binary $N_2 - CH_4$ modelling conducted by Predescu et al. showed predicted azeotropic CH_4/N_2 selectivity behaviour at moderate temperatures for naturally rich Ca^{2+} Turkish clinoptilolite [53]. The temperature effects on N_2 and CH_4 adsorption on natural clinoptilolite showed increased N_2/CH_4 selectivity on natural clinoptilolite at low temperatures due to diffusion limitations of CH_4, with natural clinoptilolite being N_2 selective at 273 K [54]. Aguilar-Armenta et al. studied the adsorptive equilibria and kinetics of several light gases including CO_2, N_2, and CH_4 on partially cation exchanged clinoptilolite; with K^+ and Ca^{2+} exchanged clinoptilolite shown to be effective for kinetic separations of CO_2/CH_4 and N_2/CH_4 mixtures [55]. However, it should be mentioned that the presence of Mg^{2+} cations in these partially exchanged samples may have contributed to the observed kinetic selectivity as observed in previous studies [11,12]. Jayaraman et al. studied the effects of single and mixed cations including Mg^{2+}, Na^+, Ca^{2+}, Li^+, Sr^{2+} and Ce^{3+} exchanged clinoptilolites on N_2 and CH_4 adsorption equilibria and kinetic uptake [50,56]. These results showed that several different ion exchange combinations including partially exchanged mixed Na^+/Mg^{2+}, Ca^{+2}/Mg^{+2}, and Na^+/Li^+ cations induce favourable kinetic

and equilibrium N_2/CH_4 gas separations comparable to that of titanosilicate ETS-4 [50,56]. Karousos et al. showed that natural clinoptilolite shows some promise for CO_2/N_2 gas separations, with significant selectivity at a higher temperature of 403 K [57]. The effect of acid treatment on natural clinoptilolite tuff showed that H^+ ions tend to open the channels of the zeolite leading to greater CH_4 adsorption [12,58].

2. Objective

Several research contributions have demonstrated the adsorptive and diffusive properties of CO_2, CH_4, and N_2 gases on various natural and cation exchanged clinoptilolites. These studies have been limited to modification using naturally occurring cations (Na^+, K^+, Mg^{2+}, and Ca^{2+}) with some other cations including Li^+, Ce^{3+}, and Sr^{2+}. The type of charge balancing cation influences the effective pore size of this zeolite, and the acid-base properties of the zeolitic framework.

This study attempts to build on work of previous systemic screening studies of this type [9–11,50,59]. In this work, natural and several different cation exchanged clinoptilolites were analyzed in order to screen for potential equilibrium and diffusion selective characteristics for CO_2, CH_4 and N_2 gases. Clinoptilolite was modified with three different groups of cations; alkali metals, alkaline earth metals, and transition metals. Single gas CO_2, CH_4, and N_2 adsorption isotherms and kinetic adsorptive uptake curves were measured using the gravimetric method at 303 K to identify the most promising cations to be used for these separations.

3. Materials and experimental methods

3.1. Materials

Natural clinoptilolite zeolite tuff originating from deposits in Nevada, USA was purchased from Ash Meadows Zeolite LLC. (Amargos Valley, NV.). The clinoptilolite was received as +140 US. Std. mesh powder. The skeletal density of the raw clinoptilolite was assessed to be 2.12 g cm^{-3} using a Micromeritics volumetric adsorption analyser and helium gas as the probe gas. The cation exchange salt solutions were prepared using deionized water and cation containing reagent salts as presented in Table 3. Where possible, salts containing chloride ions as the counterbalancing negative ion for each reagent were used to reduce the risk of additional variation within the screening process.

Single gas adsorption experiments were conducted using high purity CO_2, N_2, and CH_4 gases; high purity He gas was used for buoyancy correction for the single gas adsorption isotherm experiments. All gases purchased from Linde Canada Ltd. (Ottawa, Canada) and had the following specifications for purity: 99.995% He, 99.99% N_2, 99.99% CH_4, and 99.99% CO_2.

3.2. Preparation of cation exchanged clinoptilolites

The preparation of the adsorbent prior to cation exchange was carried out in a similar fashion as described in the literature [11,50,56]. The raw clinoptilolite powder was mixed with deionized water with a ratio of 1 g of clinoptilolite to 80 mL of deionized water. The mixture was heated to between 80 °C and 90 °C under minimal agitation for a minimum of 1 h. Following this step, the solution is decanted and the remaining clinoptilolite is rinsed with 50 mL of deionized water, this step is repeated twice to ensure that the raw clinoptilolite is purified of any undesirable soluble salts. The washed clinoptilolite was then placed in an oven and dried at 105 °C overnight.

In a 50 mL Teflon lined autoclave; a ratio of 1 g of the washed dry clinoptilolite was mixed with 50 mL of 0.2 M cation salt solution. The amount of exchangeable cations with the clinoptilolite is in excess with this ratio of solution to clinoptilolite at this concentration [56]. The autoclave is put into the oven while it is at room temperature and

Table 3
Cation sources and reagent supplier information used in this study.

Exchangeable Cation	Chemical Reagent	Purity	Supplier
Ba^{2+}	barium chloride dihydrate ($BaCl_2 \cdot 2H_2O$)	99.0%	Sigma-Aldrich Canada Co., Oakville, ON
Be^{2+}	beryllium sulfate tetrahydrate ($BeO_4S \cdot 4H_2O$)	99.0%	Sigma-Aldrich Canada Co., Oakville, ON
Ca^{2+}	calcium chloride ($CaCl_2$)	96.0%	EMD Chemicals Inc., Gibbstown, NJ
Ce^{3+}	cerium(III) chloride heptahydrate ($CeCl_3 \cdot 7H_2O$)	98.0%	Sigma-Aldrich Canada Co., Oakville, ON
Cs^+	cesium chloride ($CsCl$)	99.0%	Sigma-Aldrich Canada Co., Oakville, ON
Cu^{2+}	copper(II) sulfate pentahydrate ($CuO_4S \cdot 5H_2O$)	98.0%	Sigma-Aldrich Canada Co., Oakville, ON
H^+	hydrochloric acid (HCl)	37% solution	Acros Organics, Geel, Belgium
Fe^{3+}	iron(III) chloride hexahydrate ($FeCl_3 \cdot 6H_2O$)	99.0%	BDH Inc., Toronto, ON.
Li^+	lithium chloride ($LiCl$)	99.0%	Fisher Scientific Company, Ottawa, ON.
Mg^{2+}	magnesium chloride hexahydrate ($MgCl_2 \cdot 6H_2O$)	99.0%	Fisher Scientific Company, Ottawa, ON.
Na^+	sodium chloride ($NaCl$)	99.0%	Anachemia Canada Inc., Montreal, QC
Ni^{2+}	nickel(II) chloride hexahydrate ($NiCl_2 \cdot 6H_2O$)	99.9%	Sigma-Aldrich Canada Co., Oakville, ON
K^+	potassium chloride (KCl)	99.0%	Sigma-Aldrich Canada Co., Oakville, ON
Rb^+	rubidium chloride ($RbCl$)	99.0%	Sigma-Aldrich Canada Co. Oakville, ON
Sr^{2+}	strontium chloride hexahydrate ($SrCl_2 \cdot 6H_2O$)	99.0%	Sigma-Aldrich Canada Co. Oakville, ON
Zn^{2+}	zinc(II) sulfate heptahydrate ($ZnO_4S \cdot 7H_2O$)	99.0%	Fisher Scientific Company, Ottawa, ON.

heated in the oven to 135 °C for 10 h. Then it is removed from the oven and is cooled to room temperature over 2 h under ambient conditions. The 0.2 M salt solution is then decanted, leaving behind partially cation exchanged clinoptilolite.

The procedure indicated in the above paragraph is repeated once more to increase the exchange of the cations into the clinoptilolite. Following the decanting of the exchange solution, the clinoptilolite is rinsed twice with 50 mL of deionized water, and dried at 105 °C for 24 h and cooled down to room temperature. Afterwards, the clinoptilolite is activated at 300 °C.

3.3. Sample characterization

The purity of the original natural clinoptilolite sample was verified through x-ray diffraction (XRD) analysis. The powdered samples were examined at room temperature using a Rigaku Ultima IV powder diffractometer in Bregg-Brentano geometry, using Cu Kα radiation (λ = 1.5418 A). The 2θ range of 2°–90° was covered with a 0.02° step width and 6°/min scan speed. The XRD diffraction patterns were analyzed using the Rietveld refinement method and X'Pert Highscore Plus analysis software. The diffraction patterns of the samples were compared to the characteristic patterns for clinoptilolite established by the International Zeolite Society (IZA) [60].

Electron Dispersive Spectroscopy (EDS) analysis was used to verify the atomic composition of the cation exchanged clinoptilolite samples. A JEOL JSM-6610LV series scanning electron microscope equipped

with an Oxford INCA large area SDD detector was used with the following configuration: 20 kV acceleration voltage, 10 mm working distance, and 400 μm magnification.

3.4. Single gas adsorption isotherm and uptake-rate experiments

The single gas CO_2, CH_4 and N_2 adsorption isotherms and uptake-rate measurements were performed using the gravimetric method with a microgravimetric analyser equipped with a Cahn balance from VTI Corp. (Hialeah, Florida, USA) following a similar method as our previous study [61]. This equipment allows for the concurrent monitoring of both the static equilibrium and dynamic adsorption uptake measurements. Experiments were carried out using a Cahn microbalance that has an accuracy of ± 1 μg enclosed within a stainless steel chamber. The experimental temperature was controlled using a jacketed water bath installed around the adsorption chamber and was monitored using a thermocouple with an accuracy of ± 0.01 K. The samples were regenerated under high vacuum conditions of approximately 10^{-8} atm using a high vacuum turbo molecular pump at a temperature of 573 K. The samples were considered to be fully regenerated once the sample weight remained unchanged over a period of 1 h.

Following regeneration, the adsorbents were exposed to the sample gas and were evaluated at increasing pressure steps ranging from 0 to 10 atm at 303 K. For each pressure step change, the dynamic adsorption uptake was monitored and recorded as the change in sample weight as a function of time. Sufficient time was allowed for the system to reach equilibrium, which was determined to be achieved once a weight change of less than 0.015 wt% over a period of 15 min was observed, at which time the equilibrium adsorption measurement was recorded. The reversibility of the adsorption process was tested for each sample by measuring desorption isotherms and observing the sample weight change at decreasing pressure steps. The experimental sample weight was corrected for buoyancy by exposing the sample to high purity helium at similar pressures and temperatures. Since helium is a much smaller molecule than the gases used in this study, it will have access to smaller micropores than what CO_2, CH_4, and N_2 gases will have access to. Therefore, after the buoyancy correction, we will actually be reporting the excess amount adsorbed for these systems [62], and those values were fit to different isotherm models used in this study.

4. Adsorption models

4.1. Modelling of single component adsorption equilibria

If the adsorption isotherm exhibits type I behaviour as classified by Brunauer, Deming, Deming, and Teller (BDDT), the equilibrium adsorption data for each sample can be described simply with the Langmuir adsorption isotherm regression [63]. The Langmuir approach relies on the assumptions that adsorption is in a state of dynamic equilibrium, limited by a fixed number of localized adsorptive sites, with monolayer adsorption where there is no interaction between adsorbed molecules within the adsorbed sites, and that the energy of adsorption is consistent over all sites [64,65].

$$\theta = \frac{q}{q_m} = \frac{BP}{1 + BP} \qquad (1)$$

Here, θ is the fractional coverage on the adsorbent surface; q is the amount adsorbed; q_m is the saturation monolayer adsorption capacity; B is the affinity constant; and P is the pressure [16,65].

The Toth model equation carries much of the same conventions as the Langmuir approach, however it allows for greater flexibility for the prediction of adsorption systems. At very low pressures the Toth isotherm equation reduces to the Henry's law isotherm equation and is thermodynamically consistent, thus the adsorption equilibria data can be interpolated over a range of different temperatures and pressures

[16,17].

$$\theta = \frac{q}{q_m} = \frac{BP}{[1 + (BP)^n]^{\frac{1}{n}}} \qquad (2)$$

The additional n parameter is dimensionless. When the n parameter equals 1, the Toth model equation reduces to the Langmuir equation.

4.2. Modelling of adsorption kinetics

In order to interpret the adsorption transport diffusivity from the experimental kinetic uptake rate data, a diffusion model must be applied to determine the diffusion coefficients. It is important to envision the clinoptilolite as a semi-infinite plane whereby microporous gas diffusion may occur within the A, B, and C channels in a 2 dimensional pore arrangement. Differences in access to the pores is governed by the gas type and variations in the channel structure resulting from the occupation of various cations within the pores [11]. In reality the evaluation of this kinetic behaviour is fairly complicated. However, in order to rapidly quantify the kinetic uptake data for comparison purposes between different materials, a simplified approximation is undertaken using the Linear Driving Force (LDF) model as shown in Equation (3) [64,66–70].

$$\frac{\partial q}{\partial t} = k_{LDF}(q_e - q(t)) \qquad (3)$$

This approach relies on the assumption of a homogenous adsorbent media whereby the mass transfer coefficient, k_{LDF} is independent of adsorbate concentration. To apply the LDF model, the experimental pressure step change response is monitored as the amount adsorbed $q(t)$ at different times (t). The change in q as a function of time gives the slope, dq/dt, that is plotted as a function of $q(t)$ for different times. Since the q_e value is known as the amount adsorbed at equilibrium, the slope of this plot gives k_{LDF} specific to the system.

The LDF diffusion model is valid in the fractional uptake region $\frac{q(t)-q_0}{q_e-q_0}$ of between 0.6 or 0.7 and less than 0.99 [64,71]. Intracrystalline diffusion resistance within the micropores of clinoptilolite is an influential transport rate controlling mechanism. The diffusion time constant, D_e/R_p^2, is used to better reflect the effective intracrystalline diffusion within the zeolite as shown in Equation (4) [67].

$$k_{LDF} \approx \frac{15D_e}{R_p^2} \qquad (4)$$

where D_e/R_p^2 is the diffusion time constant [s^{-1}] which is the effective transport diffusivity, D_e, divided by the squared radius of the pellet, R_p.

4.3. Evaluating adsorbent separation potential

Comparison of the pure component adsorption equilibria for different gases is a first step required to assess the potential applicability of the adsorbent materials for a particular gas separation. The ideal selectivity, α, and separation factor, S, are good tools to initially screen for the most promising adsorbent materials for a particular separation process.

The ideal adsorption equilibrium separation factor is defined as the ratio of the equilibrium pure component adsorption capacities, and can be expressed as the ratio of the Langmuir isotherm parameters outlined in Equation (1) [8,72].

$$\alpha_{i,A/B} = \frac{X_A \cdot Y_B}{X_B \cdot Y_A} \approx \frac{q_{mA}B_A}{q_{mB}B_b} \qquad (5)$$

The more strongly adsorbed component is labelled with the subscript A, whereas the weakly adsorbed component is labelled with subscript B. For a gas mixture, the adsorbed phase mole fraction is denoted as X, whereas the gaseous phase mole fraction of a mixture is denoted as Y.

The adsorption equilibrium selectivity, S, is calculated using Equation (6). It is evaluated based on the ratio of the working adsorption capacities for species A and B, Δq_A and Δq_B, which is the difference in the adsorption capacity at the adsorption pressure and desorption pressure, respectively [72]. For this analysis, the adsorption working capacity ratios was assessed for pressure ranges from 0.1 to 1 atm, and from 1 to 10 atm for prospective VSA and PSA performances, respectively.

$$S = \alpha_{i,A/B}\frac{\Delta q_A}{\Delta q_B} \qquad (6)$$

The narrow channels of small pored structured clinoptilolite zeolites coupled with the variable cation exchange positions located within the channels offer the possibility of a kinetically driven separation. The kinetic selectivity, $K_{A/B}$, is employed to approximate separation performance based on the diffusivity ratio (which is the same as the ratio of kinetic mass transfer coefficients) determined from Equations (3) and (4), and the ideal adsorption equilibrium separation factor calculated for two different adsorbed components (Equation (7)) [8,73].

$$K_{A/B} = \alpha_{i,A/B}\sqrt{\frac{k_{LDF_A}}{k_{LDF_B}}} \qquad (7)$$

5. Results and discussion

5.1. Compositional analysis

The composition of the modified clinoptilolite samples were analyzed using EDS. The results are compared to the raw clinoptilolite and are presented in Table 4. In this table, the elemental composition is normalized to the approximated amount of aluminum atoms present in the unit cell for clinoptilolite. The total amount exchanged is quantified as the percent difference between the natural occurring cations (K$^+$, Ca^{2+}, Mg^{2+}) present in the exchanged clinoptilolite sample compared to those present in the original raw clinoptilolite sample.

As can be seen in Table 4, following the cation exchange procedure, a significant portion of the naturally occurring exchangeable cation types present in the raw sample were substituted. These results suggest that a high proportion of non-native cations are capable of occupying the channels of the zeolite, which is consistent with previous studies that indicated an overall high potential exchangeability of the extra-framework cations [74]. The Si/Al ratio of the raw zeolite sample is 5.10 and follows the range reported in the literature for clinoptilolite [32,75]. Due to limited EDS detector probe sensitivity, the atomic compositions for the H$^+$, Li$^+$ and Be^{2+} cations are unquantified. Comparisons may be drawn with previous studies which showed sufficient Li$^+$ cation exchangeability and tendency to occupy the M(4) position in the middle of channel B (see Fig. 1), with no indication of incorporation within the lattice structure of the clinoptilolite [50,54]. Neglecting the results of the H$^+$, Li$^+$ and Be^{2+} cation exchanged samples, the average silicon to aluminum ratio of all of the cation exchanged samples 5.05 ± 0.25, and is similar to the raw sample. The Fe^{3+} cation exchanged sample presents a high silicon to aluminum ratio of 5.85, indicating a decrease in the absolute amount of aluminum present compared to the raw clinoptilolite.

5.2. Structural screening analysis

The XRD pattern of the raw and modified clinoptilolite samples are presented in Fig. 2. The samples were compared visually to the characteristic patterns identified in the literature for clinoptilolite minerals [35,76,77]. The crystal structure was assessed using the Rietveld method provided in X'Pert Highscore Plus Software [78]. This interpretation showed that the original material is primarily composed of clinoptilolite (71 wt%). The remaining portion of the mineral phase

Table 4
Unit cell elemental composition of prepared clinoptilolite samples obtained using EDS.

SAMPLE	Cation	atoms/unit cell								% of Natural Cations Exchanged[b]	Si:Al
		O	Al	Si	K	Ca	Mg	Fe	Exchanged Cation		
raw clinoptilolite	–	111.19	6.00	30.65	1.49	1.68	0.71	0.27	–	–	5.10
acid treated clinoptilolite[a]	H^+	128.30	6.00	39.53	0.46	0.83	0.46	–	a	57.8	6.59[a]
Li – clinoptilolite[a]	Li^+	140.47	6.00	43.10	0.76	1.36	0.53	0.05	a	34.9	7.18[a]
Na – clinoptilolite	Na^+	103.36	6.00	31.96	1.09	0.90	–	–	3.46	52.1	5.32
K– clinoptilolite	K^+	101.98	6.00	28.87	4.79	0.89	0.32	0.09	4.79	68.6	4.81
Rb – clinoptilolite	Rb^+	112.69	6.00	29.49	–	1.35	–	0.28	4.24	60.7	4.91
Cs – clinoptilolite	Cs^+	115.87	6.00	31.20	0.38	1.12	–	0.29	5.60	56.7	5.20
Be – clinoptilolite[a]	Be^{2+}	103.08	6.00	29.97	0.69	1.04	0.57	0.24	†	39.0	5.00†
Mg– clinoptilolite	Mg^{2+}	109.03	6.00	31.28	0.58	1.15	2.18	–	2.18	58.4	5.21
Ca – clinoptilolite	Ca^{2+}	98.46	6.00	29.72	0.54	3.23	0.50	0.41	3.23	65.1	4.95
Sr – clinoptilolite	Sr^{2+}	117.51	6.00	29.86	0.38	1.26	–	0.15	2.16	56.7	4.98
Ba – clinoptilolite	Ba^{2+}	110.01	6.00	31.15	0.35	0.67	0.19	0.09	3.18	68.6	5.19
Fe – clinoptilolite	Fe^{3+}	123.55	6.00	35.10	0.51	0.21	–	1.94	1.94	82.5	5.85
Ni – clinoptilolite	Ni^{2+}	116.98	6.00	31.20	–	0.68	–	0.51	5.15	71.3	5.20
Cu – clinoptilolite	Cu^{2+}	110.76	6.00	31.76	0.74	0.86	–	–	2.39	61.6	5.29
Zn – clinoptilolite	Zn^{2+}	98.54	6.00	29.65	0.84	0.99	–	–	3.68	56.0	4.94
Ce – clinoptilolite	Ce^{3+}	122.89	6.00	30.98	0.60	0.83	0.55	0.14	1.11	48.9	5.16

[a] Limited EDS detector sensitivity was not capable of accurately measuring the exchanged cation.

[b] Quantified as the % difference between the natural cations (K^+, Ca^{2+}, Mg^{2+}) present in the exchanged clinoptilolite sample compared to those present in the raw clinoptilolite sample.

consisted mostly of stilbite (18 wt%) with smaller quantities of mordenite, quartz type material, and other alumina silicate impurities such as feldspar identified. The material is monoclinic with the lattice unit cell parameters of the raw sample having the following measurements: $a = 14.6 \pm 4.0$ Å, $b = 10.9 \pm 4.0$ Å, $c = 9.1 \pm 0.5$ Å and $\beta = 109.6 \pm 12.3°$. The measured lattice parameters of the material differ from the accepted cell parameters for clinoptilolite which are: $a = 17.662$ Å, $b = 17.991$ Å, $c = 7.407$ Å and $\beta = 116.4°$ [33], and may be explained by the presence of the natural impurities of the different phases within the sample. The measured purity was considered sufficient for the screening study, particularly since mordenite is the only impurity known to exhibit significant gas adsorption tendencies and the quantity of mordenite was low and consistent across all the experimental data set.

Distinctions between the XRD profiles of the raw clinoptilolite and the cation exchanged samples shows that cation exchange appears to alter the position and intensity of some of the characteristic peaks. Small changes in the arrangement of the structure of the clinoptilolite and/or the atomic positions within the unit cell may be inferred by the differences presented in the diffraction patterns. Detailed analysis of the crystal structure have been the subject of several research contributions [42,47,48,79–81], as such this was beyond the scope of this study.

Some changes with respect to the peak intensity of the diffractograms given in Fig. 2 may be explained by the properties of the cations given in Table 5. Substitution of the cations with a higher charge to ionic radius ration, such as H^+, Li^+, Be^{2+}, Mg^{2+}, and Fe^{3+} results in

Table 5
Physical properties of the exchanged cations [82,83].

Group	Cation	Effective Ionic Radius (Å)	Hydrated Radius (Å)	Charge to Ionic Radius Ratio
–	H^+	~0.10	0.25	~10.0
alkaline earth metal	Be^{2+}	0.45	1.05	4.44
transition metal	Al^{3+}	0.53	1.25	5.66
transition metal	Fe^{3+}	0.55	1.40	5.45
transition metal	Ni^{2+}	0.69	1.35	2.89
alkaline earth metal	Mg^{2+}	0.72	1.50	2.78
transition metal	Cu^{2+}	0.73	1.35	2.74
transition metal	Zn^{2+}	0.74	1.35	2.70
alkali metal	Li^+	0.76	1.45	1.32
alkaline earth metal	Ca^{2+}	1.00	1.80	2.00
transition metal	Ce^{3+}	1.01	1.85	2.97
alkali metal	Na^+	1.02	1.80	0.98
alkaline earth metal	Sr^{2+}	1.18	2.00	1.69
alkaline earth metal	Ba^{2+}	1.35	2.15	1.48
alkali metal	K^+	1.38	2.20	0.72
alkali metal	Rb^+	1.52	2.35	0.66
alkali metal	Cs^+	1.67	2.60	0.59
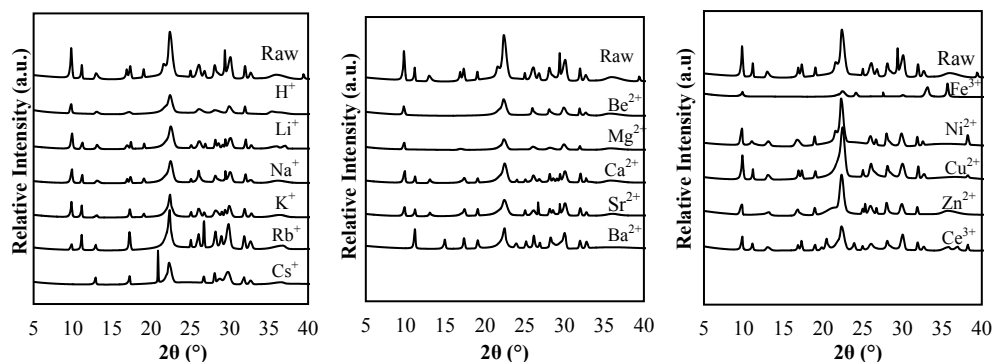
Fig. 2. Experimental XRD patterns for the raw and prepared cation exchanged clinoptilolite samples obtained at room temperature. The peak intensity patterns were used to quantify the structural purity and unit cell lattice parameters of the samples.
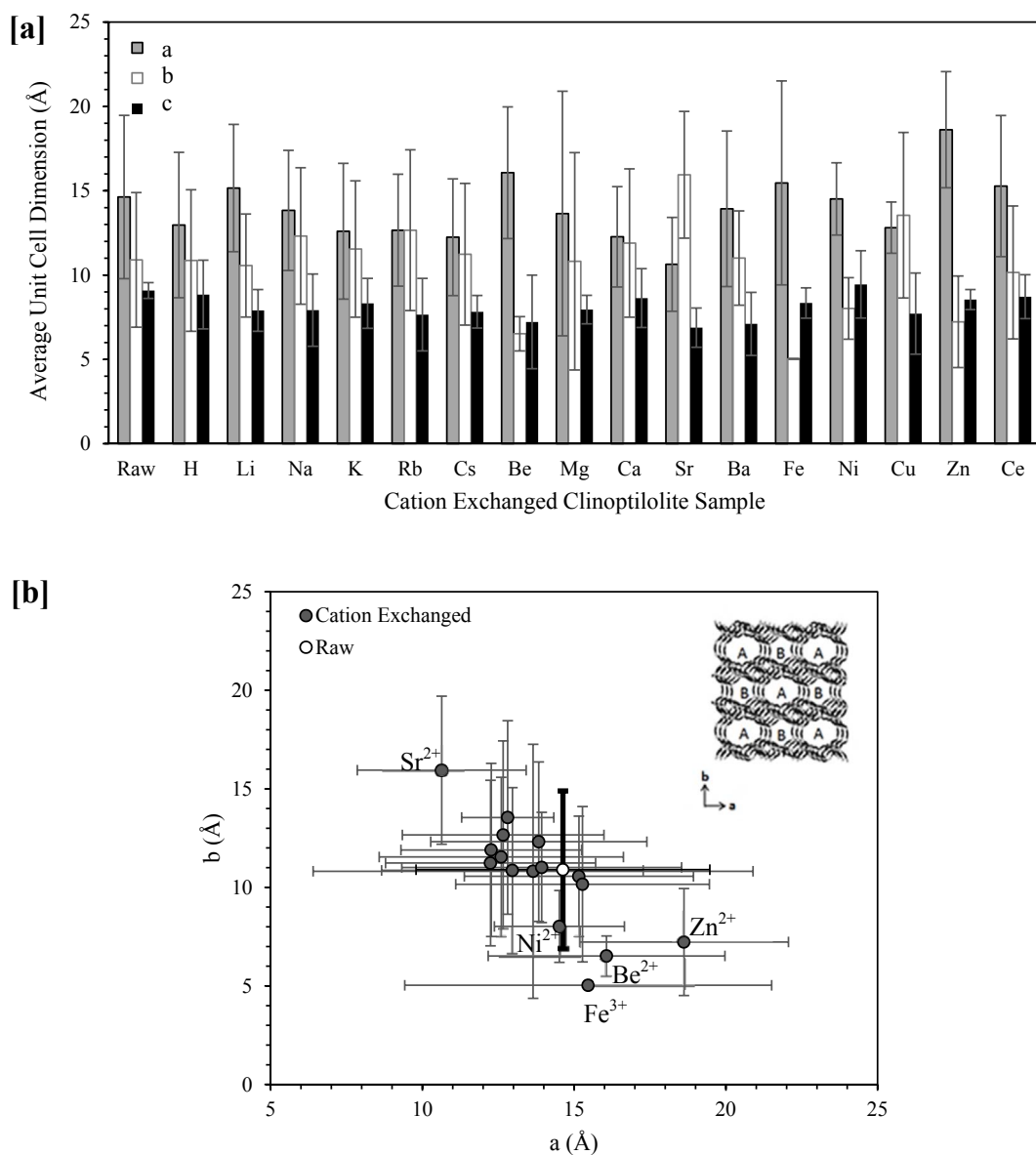
Fig. 3. [a]Experimentally determined lattice dimensions of the prepared clinoptilolite samples compared to raw clinoptilolite determined using the Rietveld refinement method on XRD powder patterns at room temperature. [b] Comparison of experimentally determined lattice dimensions in the a – b axis determined from the Rietveld refinement method on XRD powder patterns at room temperature.

less defined diffraction patterns. This likely indicates a change in the atomic density and increased disorder resulting in generally lower crystallinity of the zeolite framework [75]. These patterns may also be partially caused by the relative acidity attributed to ion exchange environment, as demonstrated by Alver and Sakizci where a loss of crystallinity was observed with increasing HCl concentrations in the exchange environment [58]. The lowest peak intensities are observed for the clinoptilolite exchanged with Fe^{3+} cations indicating increased framework disorder.

The XRD diffraction patterns presented in Fig. 2 were analyzed using Rietvelt refinement analysis, and the dimensions of lattice parameters for the unit cell were evaluated for all of the different clinoptilolite samples as shown in Fig. 3[a] and 3[b]. The majority of the cation exchanged structural dimensions are fairly consistent with respect to the original raw clinoptilolite sample given the precision of this screening method. The most significant change in the unit cell lattice parameters with respect to the different cation exchanged samples are observed for the *a* and *b* directions. These coordinates follows along the same plane as channels A and B as presented in Fig. 1. This observation

is the most evident for clinoptilolite exchanged with the smaller cations, including Be^{2+}, Fe^{3+}, Zn^{2+}, and Ni^{2+} where the lattice measurements show a reduction in the b direction.

5.3. Pure component CO_2, CH_4, and N_2 adsorption equilibria

Physical adsorption is governed by the der Waals forces of dispersion and repulsion, and the electrostatic interactions which comprise of polarizability, dipole and quadrupole interactions the effect of which are largely influenced by the degree of energetic heterogeneity of the zeolite surface [64]. With respect to small pored zeolites such as clinoptilolite, physical adsorption is also influenced by steric effects with respect to access to the zeolite pore network. The capability of a broad variation in the adsorption equilibria for different gases on clinoptilolite is due to the positioning and type of extra-framework cations located within the zeolite channels [49]. In addition, the cation charge, size, and location in relation to the framework influences the available surface area and local acid sites on the surface of the zeolite.

Experimental equilibrium adsorption isotherms of pure CO_2 CH_4,

Table 6
Langmuir and Toth isotherm model parameters for pure component nitrogen, methane, and carbon dioxide adsorption isotherms on prepared cation-exchanged clinoptilolite samples at 303 K.

ion-exchanged clinoptilolite sample		Langmuir Isotherm Parameters						Toth Isotherm Parameters								
		nitrogen		methane		carbon dioxide		nitrogen			methane			carbon dioxide		
		q_m (mmol·g^{-1})	B (atm^{-1})	q_m (mmol·g^{-1})	B (atm^{-1})	q_m (mmol·g^{-1})	B (atm^{-1})	q_m (mmol·g^{-1})	B (atm^{-1})	n (-)	q_m (mmol·g^{-1})	B (atm^{-1})	n (-)	q_m (mmol·g^{-1})	B (atm^{-1})	n (-)
raw clinoptilolite		0.721	0.686	1.019	1.154	1.579	4.958	1.178	1.184	0.474	1.087	1.425	0.482	2.168	513.0	0.288
Acid treatment	H^+	0.925	0.263	1.077	0.706	2.049	1.893	4.325	0.391	0.281	1.454	1.245	0.549	2.904	318.7	0.269
exchanged alkali metal +1 cations	Li^+	0.607	0.470	0.594	0.835	1.916	3.760	1.880	1.822	0.279	0.692	1.211	0.680	2.632	1507	0.253
	Na^+	0.987	0.597	1.095	1.149	1.861	5.778	1.277	0.858	0.611	1.162	1.431	0.816	2.042	223.1	0.416
	K^+	0.959	0.522	1.216	1.276	1.813	2.997	1.094	0.765	0.605	1.436	2.517	0.606	1.950	219.8	0.396
	Rb^+	0.701	0.363	0.823	1.148	1.691	2.647	0.809	0.396	0.767	0.966	2.056	0.629	1.940	221.29	0.348
	Cs^+	0.387	0.177	0.423	0.995	1.501	2.369	0.575	0.201	0.604	0.519	1.841	0.594	1.894	261.1	0.316
exchanged alkaline earth metal +2 cations	Be^{2+}	0.615	0.470	0.939	0.953	1.663	8.825	1.605	2.565	0.287	1.159	1.742	0.593	2.118	305.9	0.342
	Mg^{2+}	0.702	0.585	0.946	1.061	1.819	3.773	2.110	4.394	0.259	1.189	2.341	0.540	2.148	284.5	0.332
	Ca^{2+}	0.680	0.370	0.329	0.557	1.601	8.443	1.682	2.301	0.275	0.393	1.679	0.582	2.108	266.1	0.330
	Sr^{2+}	0.915	1.143	1.119	3.254	1.861	6.868	1.368	6.099	0.398	1.250	6.246	0.621	2.010	154.7	0.421
	Ba^{2+}	1.001	1.712	1.140	3.329	1.825	6.462	1.761	13.46	0.329	1.286	6.308	0.640	2.007	267.9	0.401
exchanged transition metal cations	Fe^{3+}	0.654	0.190	0.855	0.653	1.341	1.967	1.076	0.165	0.607	0.992	0.826	0.718	1.789	53.92	0.342
	Ni^{2+}	0.656	0.443	0.727	0.676	1.729	2.505	2.423	1.155	0.278	1.089	1.424	0.482	1.982	157.3	0.359
	Cu^{2+}	0.492	0.433	0.654	1.381	1.453	7.031	1.930	1.344	0.262	0.799	3.519	0.548	1.494	81.02	0.462
	Zn^{2+}	0.621	0.373	0.803	0.876	1.599	3.653	1.875	0.623	0.332	0.953	1.355	0.651	1.850	38.19	0.432
	Ce^{3+}	0.511	0.501	0.799	0.952	1.533	9.526	1.742	1.750	0.274	0.938	1.520	0.653	1.862	76.19	0.431

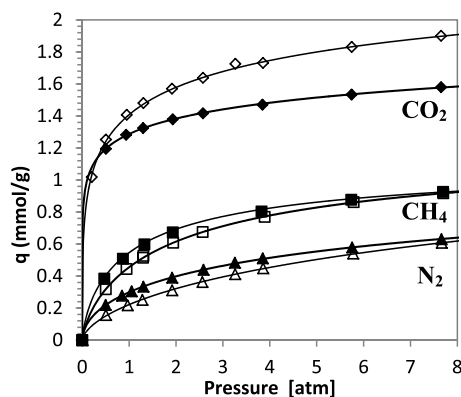**Fig. 4.** Experimentally determined adsorption isotherms with Toth model fit for CO_2, N_2, and CH_4 at 303 K for raw clinoptilolite (filled points) and 0.2 M HCl acid treated clinoptilolite samples (open points).

and, N_2 gases on the different cation exchanged clinoptilolites were performed as described in Section 3.4. In general, the adsorption equilibria data for the studied gases on clinoptilolite can be considered as type I adsorption isotherms as classified by BDDT over the experimental pressure range [63]. Therefore, Langmuir and Toth isotherm models were employed on the experimental data, and the corresponding parameters are presented in Table 6.

5.3.1. Raw and acid treated clinoptilolite

Raw clinoptilolite consists of different types of naturally occurring cations whose quantity and proportions depend on the local source of the mineral deposits. The raw clinoptilolite used in this study consisted of a distribution of Ca^{2+}, K^+, Mg^{2+}, and Fe^{3+} extra framework cations. Fig. 4 shows that the observed adsorption equilibria follows the expected trend with CO_2 as the most readily adsorbed component, followed by CH_4 and N_2. The greater adsorption equilibrium capacity for CH_4 compared to N_2 indicates that access to the pore network is not impeded by the distribution of the naturally occurring cations in the raw sample for the larger CH_4. While the Ca^{2+} cation has been shown to successfully block access of CH_4 gas to the pore network [51], there exists insufficient quantities of Ca^{2+} cation present in the natural sample for this to occur.

Acid treatment results in partial replacement of the naturally occurring cations occupying the channels of the zeolite, thereby opening up access to the channels for adsorption to occur [49,58]. Differences may be observed with respect to the adsorption equilibria capacity of the acid treated clinoptilolite compared to the raw clinoptilolite. At higher pressures CO_2 capacity is greater for the acid treated clinoptilolite, whereas CH_4 and N_2 adsorption capacities of the acid treated clinoptilolite are approximately equivalent to that of the raw clinoptilolite sample.

5.3.2. Alkali metal cation exchanged clinoptilolite

Fig. 5 presents the single gas adsorption equilibrium isotherms for CO_2, CH_4, and N_2 gases performed at 303 K on the alkali metal cation exchanged clinoptilolite samples. In all cases, the observed adsorption equilibria capacities follow the expected trend of $CO_2 > CH_4 > N_2$. Adsorption of CO_2 follows the trend in the ionic radii of the substituted cations, where CO_2 adsorption capacity is observed follow the order of: $Li^+ \approx Na^+ > K^+ > Rb^+ > Cs^+$, with Cs^+ being the largest cation and Li^+ being the smallest (see Table 5). Similar trends in CO_2 adsorption capacity were observed for other small pored zeolites exchanged with alkali cations including: chabazite [22], zeolite beta [84], zeolite X and zeolite Y [85]. It is thought that the greater electrostatic charge density of the smaller cations results in higher surface potential. In addition, smaller cations take up smaller space in the channels opening up more space for molecules to be adsorbed. The net result is
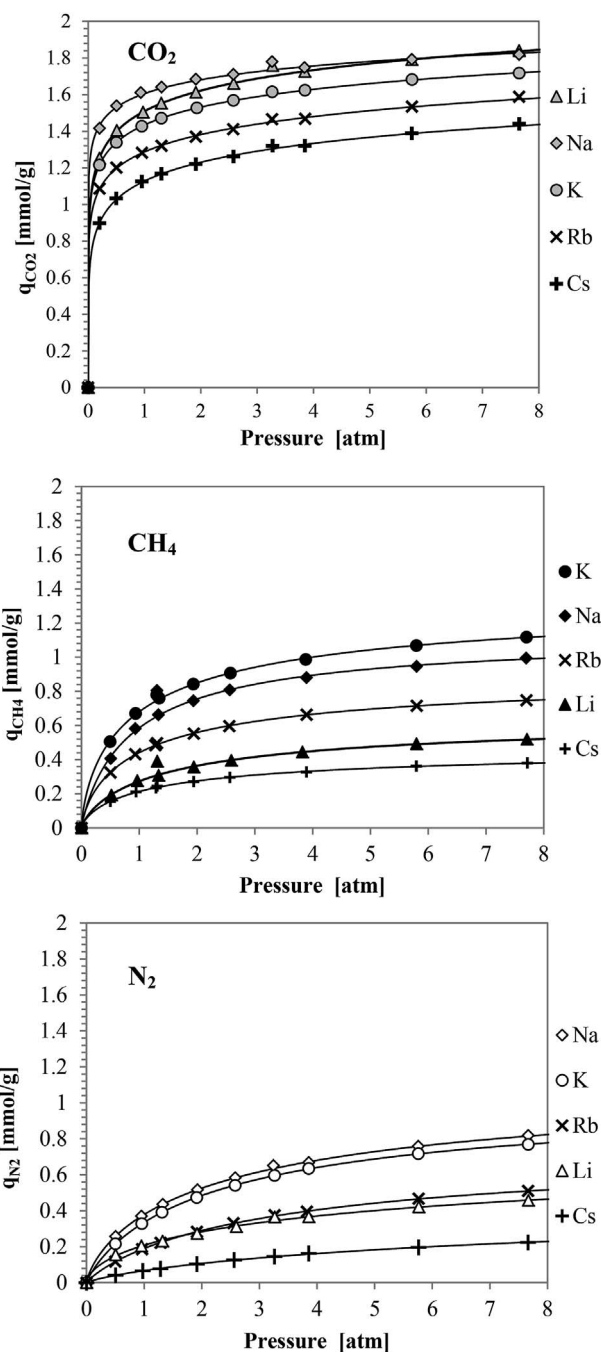

Fig. 5. Experimentally determined adsorption isotherms with Toth model fit for CO_2 (top), CH_4 (middle) and N_2 (bottom) at 303 K for acid treated and alkali +1 cation exchanged clinoptilolite samples.

greater adsorption potential for CO_2 [22]. The presence and size of these cations within the channel cavity also follow the expected trends with the larger cations occupying a greater space thus limiting the absolute amount of CO_2 adsorbed.

The CH_4 adsorption equilibria were greater than that of N_2, with the order of CH_4 adsorption equilibria being: $K^+ > Na^+ > Rb^+ > Li^+ > Cs^+$ for the alkali cation exchanged samples. This compares to N_2 adsorption equilibria capacity being in the order of: $Na^+ > K^+ > Rb^+ > Li^+ > Cs^+$. Yang and Armbruster studied the crystal structure of alkali metal cation exchanged heulandite. They confirmed the existence of cation coordinated positions for Rb^+ and Cs^+ adjacent to the framework in the 10 member ring in channel A, and within the centre of the 8 member ring in channel B [36]. Importantly,

this means that the Mg^{2+} cations originally occupying the M(4) position in the middle of channel A are completely removed following cation exchange (see Table 4). Therefore, channel A is open and facilitates access of the studied gas molecules to the inner channels of the zeolite for adsorption. In comparison Li^+ is the smallest of the alkali cations, however the Li^+ exchanged clinoptilolite shows a lower adsorption capacity for both N_2 and CH_4 than most of the other alkali cations. This effect may be explained by also considering the presence of the natural Ca^{2+}, Mg^{2+}, and K^+ cations present in the Li^+ exchanged sample (see Table 4). It is likely that coordination of the Li^+ cations with the natural cations results in occupying positions within the channels which limits access to the studied CH_4 and N_2 gases.

The composition and distribution of the naturally occurring cations within the original starting clinoptilolite sample affects the adsorption properties of the sample following cation exchange. In this study, the parent clinoptilolite sample contained a distribution of Ca^{2+}, K^+, Mg^{2+}, and Fe^{3+} cations, with no Na^+ cations. Kouvelos et al. showed that samples originally rich in Na^+ cations and treated with an acid bath prior to the Li^+ cation exchange procedure showed higher uptake of CH_4 and N_2 compared to Na^+ form of clinoptilolite [54]. Natural clinoptilolite originally rich in Ca^{2+} cations and exchanged with Na^+ cations resulted in a reduced equilibrium adsorption capacity for CH_4 and inverse N_2/CH_4 selectivity [56].

5.3.3. Alkaline earth metal cation exchanged clinoptilolite

Fig. 6 presents the single gas adsorption equilibrium isotherms performed at 303 K for CO_2, CH_4, and N_2 gases on the alkaline earth metal cation exchanged samples. The alkaline earth metal cation exchanged clinoptilolite samples exhibit different gas adsorption behaviour compared to the alkali metal cation exchanged samples. The sequence of CO_2 adsorption for the different cation exchanged samples are as follows: $Ba^{2+} > Sr^{2+} \gg Be^{2+} \approx Mg^{2+} > Ca^{2+}$. Similar trends are exhibited with the N_2 equilibrium adsorption capacity where the order of the adsorption capacity is as follows: $Ba^{2+} > Sr^{2+} \gg Mg^{2+} > Be^{2+} > Ca^{2+}$. Differences in CO_2 adsorption capacity were lower than those for CH_4 and N_2 gases.

The Ba^{2+} and Sr^{2+} cation exchanged clinoptilolite samples both have a noticeably higher adsorption capacity for all three studied gases compared to the exchanged samples with the three smaller alkaline earth cations. These two alkaline earth cations occupy different positions in the clinoptilolite than the smaller Mg^{2+}, Be^{2+}, and Ca^{2+} cations. Previous research contributions have shown that the Ba^{2+} cations occupy spaces adjacent to the framework in the vicinity of the M(1) and M(3) positions [41,86]. Similar observations have also been found for Sr^{2+} cations, with a greater preference for the M(1) position [87]. Since these cations occupy areas closer to the side of the channel, rather than the middle of it, the overall cavity volume accessible to the studied gases is likely higher. Additionally, the positioning of the Sr^{2+} and Ba^{2+} cations in the M(1) site and the large hydrated radii of these cations (Table 5) results in displacement and reduction of the Mg^{2+} cation (see Table 4) residing in the M(4) position, opening up channel A for gas adsorption. The result is an open channel A, which is associated with increased gas uptake during adsorption compared to the other cations.

The influence of the cation positions are demonstrated particularly with respect to the observed CH_4 adsorption equilibria where three distinct CH_4 adsorption isotherm patterns are observed in Fig. 6. CH_4 adsorption capacity is in the order of: $Ba^{2+} > Sr^{2+} \gg Be^{2+} \approx Mg^{2+} \gg Ca^{2+}$. The Ca^{2+} clinoptilolite shows effective pore blocking of the channels, thereby limiting access of the larger CH_4 gas molecules to the pores through steric hindrance, an effect which is extensively described in detail in the literature [12,51]. This results in inverse equilibrium selectivity for N_2 over CH_4. The Mg^{2+} and Be^{2+} cation exchange varieties, along with the Sr^{2+} and Ba^{2+} clinoptilolites show similar behaviour as explained for the CO_2 and N_2 adsorption equilibria.
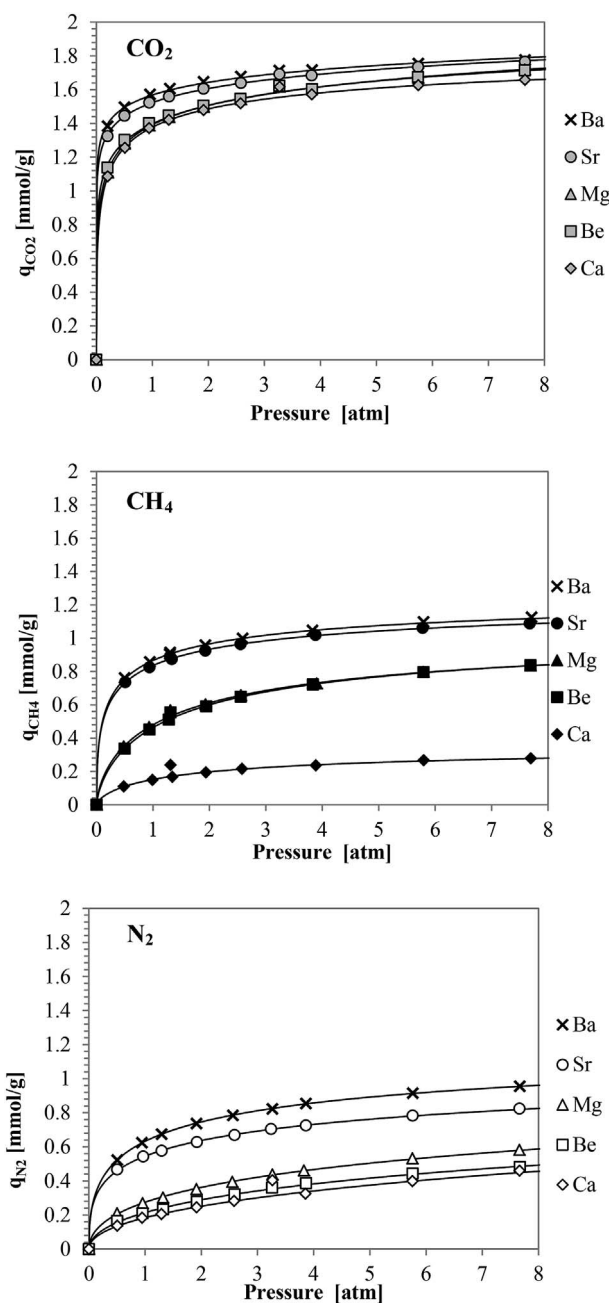

Fig. 6. Experimentally determined adsorption isotherms with Toth model fit for CO_2 (top), CH_4 (middle) and N_2 (bottom) at 303 K for alkaline earth +2 cation exchanged clinoptilolite samples.

5.3.4. Transition metal cation exchanged clinoptilolite

Fig. 7 presents the single gas adsorption equilibrium isotherms determined at 303 K for CO_2, CH_4, and N_2 gases on the transition metal cation exchanged clinoptilolite samples. The gas adsorption behaviour for these clinoptilolites is fairly complex, however some expected trends are followed such as the sequence of adsorption capacity which was $CO_2 > CH_4 > N_2$ in all cases. For each of the studied gases separately, the adsorption behaviour is confined to a narrow range on the samples exchanged with the +2 transition metal cations. It follows that these cations have very similar properties such as similar charge density and ionic radii (see Table 5).

The sequence of CO_2 adsorption for the different transition metal cation exchanged samples at higher loadings at 303 K are as follows: $Ni^{2+} \approx Ce^{3+} > Zn^{2+} > Cu^{2+} > Fe^{3+}$. Overall the differences in adsorption capacity between the different cation clinoptilolite in this
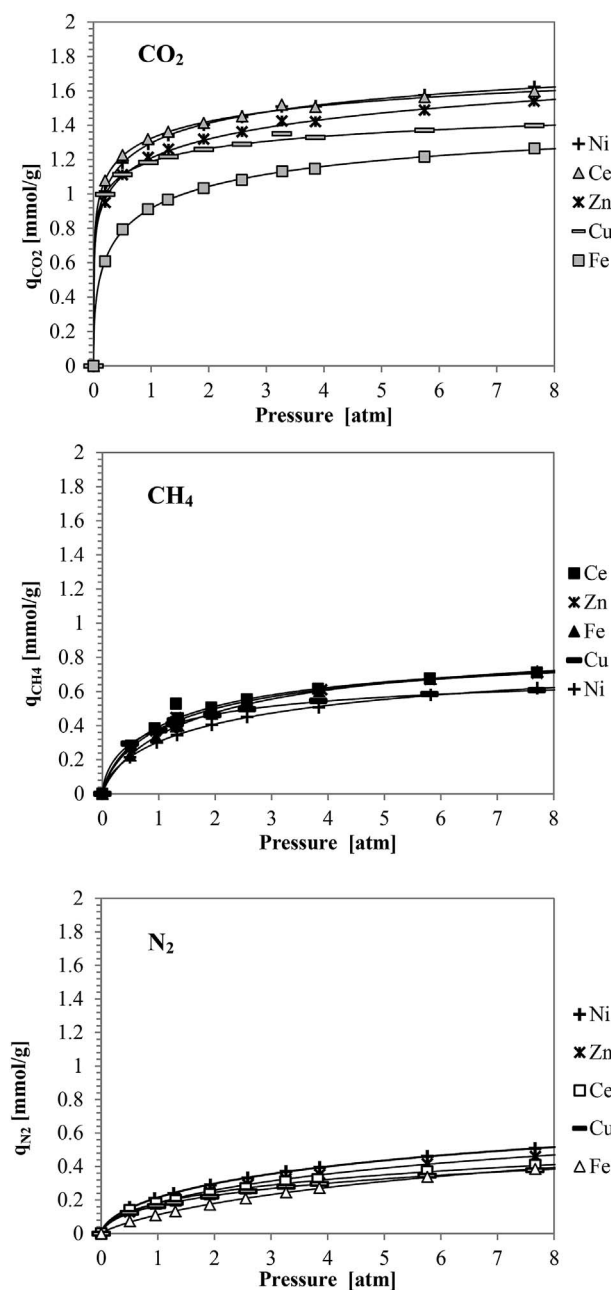
Fig. 7. Experimentally determined adsorption isotherms with Toth model fit for CO_2 (top), CH_4 (middle) and N_2 (bottom) at 303 K for transition metal cation exchanged clinoptilolite samples.

Table 7

Summary of the calculated ideal adsorption equilibrium separation factor (α) values determined from the pure component CO_2, N_2, and CH_4 isotherms at 303 K.

Cation exchanged clinoptilolite sample	$\alpha CH_4/N_2$	$\alpha CO_2/CH_4$	$\alpha CO_2/N_2$
Raw	2.4	6.7	15.8
Acid treatment H^+	3.1	5.1	15.9
Li^+	1.7	14.5	25.3
Na^+	2.1	8.5	18.2
K^+	3.1	3.5	10.9
Rb^+	3.7	4.7	17.6
Cs^+	6.1	8.4	51.9
Be^{2+}	3.1	16.4	50.8
Mg^{2+}	2.4	6.8	16.7
Ca^{2+}	0.7	73.6	53.6
Sr^{2+}	3.5	3.5	12.2
Ba^{2+}	2.2	3.1	6.9
Fe^{3+}	4.5	4.7	21.2
Ni^{2+}	1.7	8.8	14.9
Cu^{2+}	4.2	11.8	49.9
Zn^{2+}	3.0	8.3	25.2
Ce^{3+}	3.0	19.2	57.0

highest for the Ce^{3+} and Ca^{2+} exchanged clinoptilolite with a values of 57.0 and 53.6, respectively. This is over 3 times higher than the CO_2/N_2 separation factor for the raw clinoptilolite found in this work. These values are similar to those of other small pored zeolites summarized a review by Cheung and Hedin, including 4A and 5A zeolite, Li-chabazite, and zeolite T [88] and but lower than 13X zeolite [14,89]. With respect to potential CO_2/CH_4 separations, the highest CO_2/CH_4 ideal adsorption equilibrium separation factor is for the Ca^+ clinoptilolite with a value of 73.6. This value is higher compared to other small pored zeolites which range from 3 to 17 for zeolite 4A, 2 to 10 for zeolite 5A, and 2 to 8 for chabazite and H-mordenite under comparable conditions [8,90]. However, this is lower than the reported values of about 43 and 177 for CaX and 13X determined at 313 K [91]. As noted in the literature, regarding the Ca^{2+} clinoptilolite, the improved CO_2/CH_4 equilibrium separation factor comes at the expense of less desirable slower kinetics since access of the gases to the pores is restricted by the presence of the cation [54,92]. The CH_4/N_2 ideal adsorption equilibrium separation factor is the highest for the Cs^+ and Fe^{3+} exchanged clinoptilolites, with values of 6.1 and 4.5, respectively. These values are over 2 times higher than the value for the raw clinoptilolite which was 2.4. This is of particular significance since many zeolites and activated carbons reported in the literature have calculated CH_4/N_2 selectivity in the range of 1.7–5 for activated carbons, and 2.1–5 for zeolites under similar conditions [16,93–98].

The data from the presented experimental pure adsorption isotherms were then used to determine corresponding equilibrium selectivity values using Equation (6). The equilibrium selectivity values give a better idea of potential adsorbent separation performance by taking into consideration the shape of the individual isotherms as quantified by the adsorption capacity ratios at different pressures. The results are presented in Fig. 8. For this analysis, the adsorption working capacity ratios were assessed for pressure ranges of 0.1–1 atm, and 1–10 atm for separations involving CH_4/N_2, CO_2/CH_4, and CO_2/N_2. These calculated values are the highest for CO_2/N_2 separations, followed by CO_2/CH_4 and CH_4/N_2 separations.

The calculated CH_4/N_2 equilibrium selectivity values in Fig. 8 for the Fe^{3+} and Cs^+ exchanged clinoptilolites are 13.9 and 20.6, respectively, in the vacuum region, and are 5.5 and 5.7, respectively, in the higher pressure region. These values for Cs^+ and Fe^{3+} clinoptilolite is comparable to that of silicalite calculated from our previous work, which ranges from 15.8 in the vacuum region to 7.3 in the pressurized region at 303 K [61]. The Cs^+ cation has a lower charge density compared to the original Ca^{2+}, Mg^{2+}, or K^+ cations present in the raw clinoptilolite (see Table 5). As a result, increased CH_4/N_2 selectivity for Cs^+ and Fe^{3+} cation exchanged clinoptilolite could be due to greater

category were smaller compared to the other types of cation exchanged clinoptilolites, especially for CH_4 and N_2 gases.

5.4. Ideal adsorption equilibrium separation factor and selectivity

Table 7 presents the calculated ideal adsorption equilibrium separation factors (α) determined using Equation (5) with the fitted Langmuir isotherm parameters shown in Table 6. The results show the strong influence of the different exchanged cations which are capable of altering the separation factors dramatically compared to the raw clinoptilolite sample. These observed differences show that the degree of energetic surface heterogeneity (influenced by the positioning and the type of the exchanged cation), and steric factors affect the adsorption behaviour.

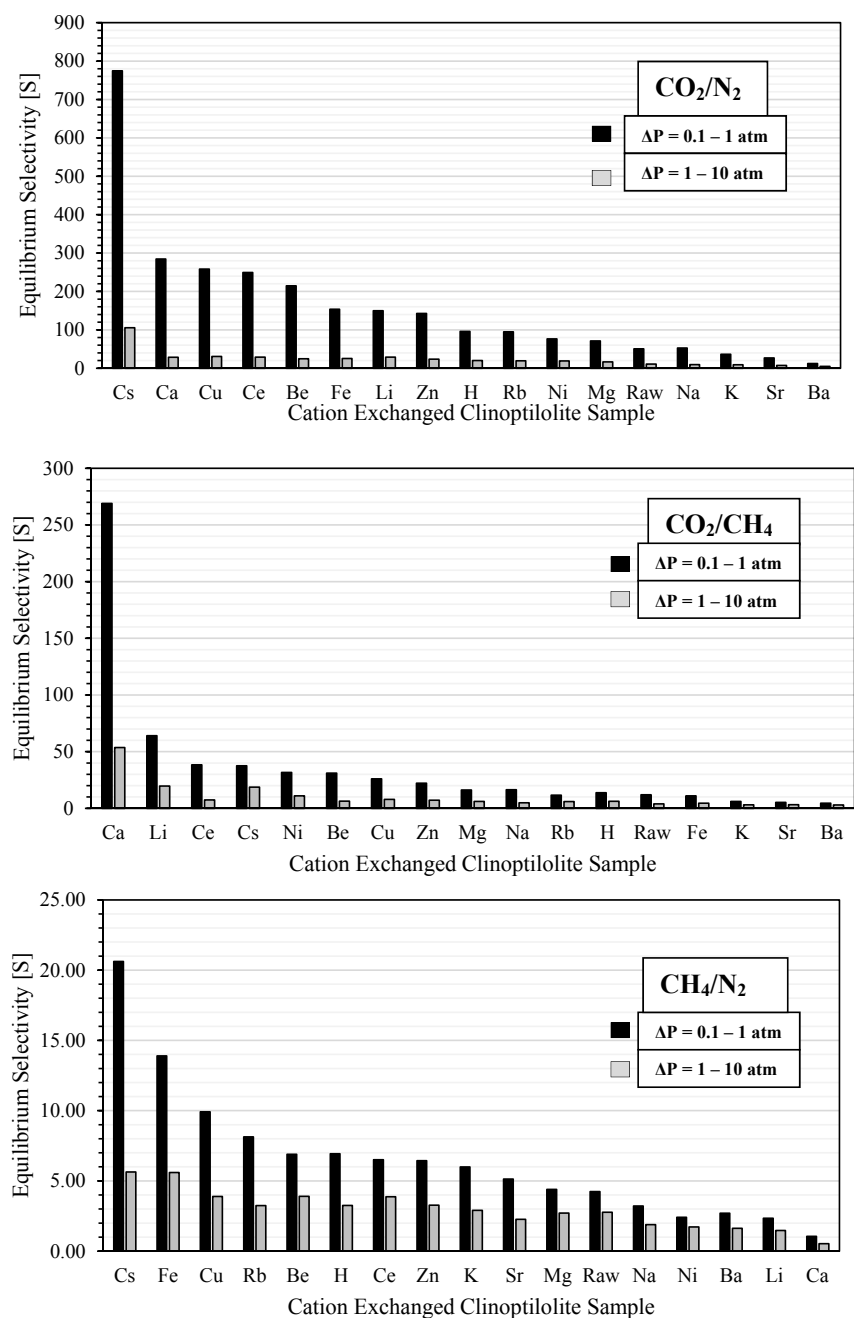The CO_2/N_2 ideal adsorption equilibrium separation factor is

Fig. 8. Experimentally determined adsorption equilibrium selectivity values for gas mixtures involving CO_2-N_2, CO_2-CH_4, and N_2-CH_4 with various prepared cation exchanged clinoptilolites at 303 K.

surface homogeneity and a lower surface charge distribution compared to the pure clinoptilolite. With respect the Fe^{3+} clinoptilolite, it is important to consider that the hydrated charge density of the Fe^{3+} cations is lower than Al^{3+} (see Table 5). Therefore possible dealumination and incorporation of Fe^{3+} cations within the zeolite lattice structure during the cation exchange procedure may result in a similar net change in the surface environment as Cs^+ clinoptilolite. A more homogeneous surface interacts with the non-polar CH_4 gas better than the N_2 gas with quadrupole moment, provided that CH_4 is not hindered by steric factors [92].

A similar explanation relates to the observed CO_2 and N_2 adsorption equilibrium selectivity shown in Fig. 8. These values are by far the highest for the Cs^+ exchanged clinoptilolite with values ranging from 770 to 105, compared to 50 to 11 for raw clinoptilolite in the vacuum region and the higher pressure region, respectively. CO_2 gas has greater than 3 times the quadrupole moment strength and higher polarizability compared to N_2 [2]. In this case, CO_2 interacts strongly with framework

surface for all of the modified clinoptilolites. The strong CO_2 surface interaction with clinoptilolite results in a much higher uptake in the vacuum region compared to N_2. This is presented as a more rectangular isotherm shape for CO_2, whereas the N_2 isotherm shape is more linear. This adsorption behaviour explains the great reduction in the experimental CO_2/N_2 equilibrium selectivity going from the vacuum region to the higher pressure region which is calculated from the CO_2 and N_2 gas working capacity values.

Additionally the CO_2/CH_4 equilibrium selectivity is also the highest for the Ca^{2+} cation exchanged clinoptilolite with values ranging from 269 to 53, in the vacuum region and in the higher pressure region, respectively. The location of the Ca^{2+} cation within the zeolite channels greatly limits the accessibility of the larger CH_4 gas molecule while not effecting the smaller CO_2 gas molecule, which explains the reduced CH_4 capacity. The same effect is also observed with respect to the Ca^{2+} clinoptilolite for potential CH_4/N_2 separations. Fig. 8 shows that the CH_4/N_2 equilibrium selectivity is 0.55 for this material (inverse value is

1.8 for the N_2/CH_4 equilibrium selectivity). This confirms that Ca^{2+} clinoptilolite is more selective for N_2 over CH_4 as reported in the literature [12,56]. However, this N_2/CH_4 equilibrium selectivity for Ca^{2+} clinoptilolite is fairly low compared to other materials reported in the literature, such as titanosilicate NaSr-ETS-4 and MIL-100(Cr) which range from 4 to 10 and 9 to 18, respectively, under similar conditions [5,29].

5.5. Kinetic adsorption modelling and N_2/CH_4 kinetic selectivity

Intra crystalline diffusion resistance is dominant in microporous zeolites such as clinoptilolite [99,100]. Therefore, it is important to understand the influence of adsorption mass transfer kinetics particularly with respect to the implications of potential diffusional limitations on possible PSA cycles [101]. Single gas adsorption uptake rates of CO_2, CH_4, and N_2 were studied on the cation exchanged clinoptilolites for a pressure step change of 0.5–1 atm at 303 K. It is important to clarify the limitations of the accuracy of the reported kinetic rate constants due to the large pressure steps used for this analysis. It is likely that a significant influence of gas flows in the initial uptake phase results in less accurate measurements. Nonetheless, since the focus of this article is to provide a ranking of adsorbent materials, the resulting fractional uptake curves were used to assess the diffusional time constant from the LDF approximation given in Equation (3) and [4]. The results are summarized in Table 8. The calculated diffusion time constants range from as low as $2.05 \times 10^{-5} \, s^{-1}$ for CH_4 diffusion in Li^+ clinoptilolite, to as high as $7.73 \times 10^{-3} \, s^{-1}$ for N_2 diffusion in Rb^+ clinoptilolite. The observed variability in diffusional uptake shows that the organization of the different cation distributions, the channel geometry, and the size of the diffusing gas effects the adsorption rate data, with N_2 (kinetic diameter = 3.6 Å) or CO_2 (kinetic diameter = 3.3 Å) being the fastest and CH_4 (kinetic diameter = 3.8 Å) having the slowest kinetics.

Fig. 9 shows the experimental adsorption uptake rate curves and LDF model fit for CO_2, CH_4, and N_2 adsorption on the raw, acid treated, and selected cation exchanged (Li^+, Fe^{3+}, Ca^{2+}) clinoptilolites. Using the raw clinoptilolite as a reference, the diffusion uptake rate follows the trend of $N_2 > CO_2 \gg CH_4$. This trend is due to the random distribution of the naturally occurring cation mixture present within the raw sample. For the raw sample, Ca^{2+} occupies the M(1) and M(2)

positions, K^+ occupies the M(3) position and Mg^{2+} occupies the M(4) position. However, none of the cations are dominant, therefore all of the channels are only partially blocked. Since the pore structure of clinoptilolite is two dimensional, this cation arrangement gives greater resistance to diffusion of the larger CH_4 molecule within the pores [10]. For the Ca^{2+} cation exchanged clinoptilolite, the increased amount of Ca^{2+} cations within channels A and B, and the continued presence of K^+ and Mg^{2+} cations (Table 4) results in limited access to the channels for both N_2 and CH_4, as indicated by the slower observed transport diffusivity. A similar channel blocking effect is observed in the case of the Li^+ clinoptilolite, whereby the cation arrangement offers little diffusional resistance to N_2 compared to CH_4. Conversely, the acid treated clinoptilolite (H^+ exchanged one) showed faster adsorption uptake for all three gases compared to the raw sample. This is reflective of the more open pore structure as a result of the acid treatment thereby decreasing the microporous diffusion resistance [44].

CH_4 is thermodynamically favoured over N_2 for adsorption equilibria onto the clinoptilolite surface. This explains the higher equilibrium adsorption capacity compared to N_2 in most cases as shown in Figs. 5–7. Nonetheless as shown in Table 7, the CH_4/N_2 equilibrium ideal adsorption equilibrium separation factor is quite modest for many of the clinoptilolite samples. Despite this limitation, some research contributions have proposed employing cation exchanged clinoptilolites for possible kinetic separations of CH_4-N_2 gas mixtures [10,11,44,50]. Since CH_4 is a larger molecule, it is more kinetically hindered than N_2 due to some of the cation positions within the channels of the two dimensional clinoptilolite structure [10,54]. This reduces the ability of the CH_4 to diffuse within the channels and access the adsorption sites. This is reflected in the order of magnitude difference in the observed adsorption rate between N_2 and CH_4 in the raw clinoptilolite, and some of its cation exchanged derivatives as shown in Table 8. The net result is that the kinetic selectivity is the reverse of the equilibrium selectivity and it favors nitrogen over methane [10,44,54,55,95,102].

In Fig. 10, the overall diffusion coefficients for Li^+, Ca^{2+}, and raw clinoptilolite are presented as a function of the total amount adsorbed for N_2 and CH_4 gases. The observed transport diffusivity values increase as loading increases for both gases (the exception being N_2 gas on raw clinoptilolite where the observed transport diffusivity decreased slightly). This trend is largely consistent with the findings of Ackley and Yang for various clinoptilolites whereby it was postulated that a combination of slow and rapid microporous diffusion occurs within the parallel channels of the clinoptilolite [11]. N_2 is the smaller gas molecule, therefore gas transport occurs more rapidly than CH_4 since it has more access to the channels that facilitate rapid transport diffusivity. Microporous materials such as clinoptilolite initially induce a resistance on the movement of gas particles. At higher loadings the transport of the gases increases due to a greater frequency of both intermolecular and surface interactions with the zeolite.

Fig. 11 presents the N_2/CH_4 ideal kinetic selectivity values calculated using Equation (7). As expected, the acid treated clinoptilolite has the lowest N_2/CH_4 kinetic selectivity (≈ 1) which can be explained by the more open pore structure of this material. The Li^+ and Ni^{2+} clinoptilolites have higher kinetic selectivity compared to the raw clinoptilolite with values of 105 and 35, respectively. In previous studies, each of Mg^{2+}, Na^+, Sr^{2+}, Ce^{3+}, and mixed Na^+-Li^+ exchanged clinoptilolites have been shown to have improved kinetic selectivity in favour of N_2 over CH_4 compared to that of natural clinoptilolite [44,50,54–56]. Both Ackley et al. and Jayaramen et al. reported that Mg^{2+} exchanged clinoptilolite had the highest kinetic N_2/CH_4 selectivity [44,56]. Jayaramen et al. also showed lower kinetic selectivity for Li^+ clinoptilolite compared to that of purified clinoptilolite which is opposite of the observed findings in this study. Importantly in those studies, the quantity of naturally occurring cations in the raw clinoptilolite starting material was in the order of $Na^+ > K^+ > Ca^{2+} > Mg^{2+}$ [50,56]. In this study, the cation content in the original raw clinoptilolite was different. The order of the naturally

Table 8
Diffusion time constants for pure nitrogen, methane, and carbon dioxide adsorption on cation-exchanged clinoptilolite samples determined at 303 K with a pressure step change from 0.5 to 1 atm using the LDF approximation.

| Ion-exchanged clinoptilolite sample		D_e/R_p^2 (s^{-1})		
		Nitrogen	Methane	Carbon dioxide
raw clinoptilolite		4.35×10^{-3}	1.12×10^{-4}	2.55×10^{-4}
Acid treatment	H^+	4.70×10^{-3}	3.83×10^{-3}	1.61×10^{-3}
exchanged alkali metal +1 cations	Li^+	3.92×10^{-3}	2.05×10^{-5}	3.50×10^{-4}
	Na^+	3.93×10^{-4}	3.44×10^{-4}	3.60×10^{-3}
	K^+	2.15×10^{-3}	7.53×10^{-4}	2.52×10^{-3}
	Rb^+	7.73×10^{-3}	6.42×10^{-4}	7.16×10^{-4}
	Cs^+	4.94×10^{-3}	4.16×10^{-4}	2.19×10^{-3}
exchanged alkaline earth metal +2 cations	Be^{2+}	2.83×10^{-3}	2.55×10^{-4}	5.32×10^{-4}
	Mg^{2+}	6.34×10^{-3}	1.37×10^{-4}	6.09×10^{-4}
	Ca^{2+}	8.39×10^{-5}	3.66×10^{-5}	1.01×10^{-4}
	Sr^{2+}	6.72×10^{-3}	5.67×10^{-4}	5.37×10^{-4}
	Ba^{2+}	2.83×10^{-3}	4.43×10^{-3}	7.41×10^{-4}
exchanged transition metal cations	Fe^{3+}	2.93×10^{-3}	2.48×10^{-3}	2.68×10^{-3}
	Ni^{2+}	4.89×10^{-3}	8.32×10^{-5}	4.29×10^{-3}
	Cu^{2+}	3.54×10^{-3}	6.46×10^{-4}	3.43×10^{-4}
	Zn^{2+}	5.47×10^{-3}	5.67×10^{-4}	5.99×10^{-4}
	Ce^{3+}	3.49×10^{-3}	5.49×10^{-5}	1.42×10^{-3}
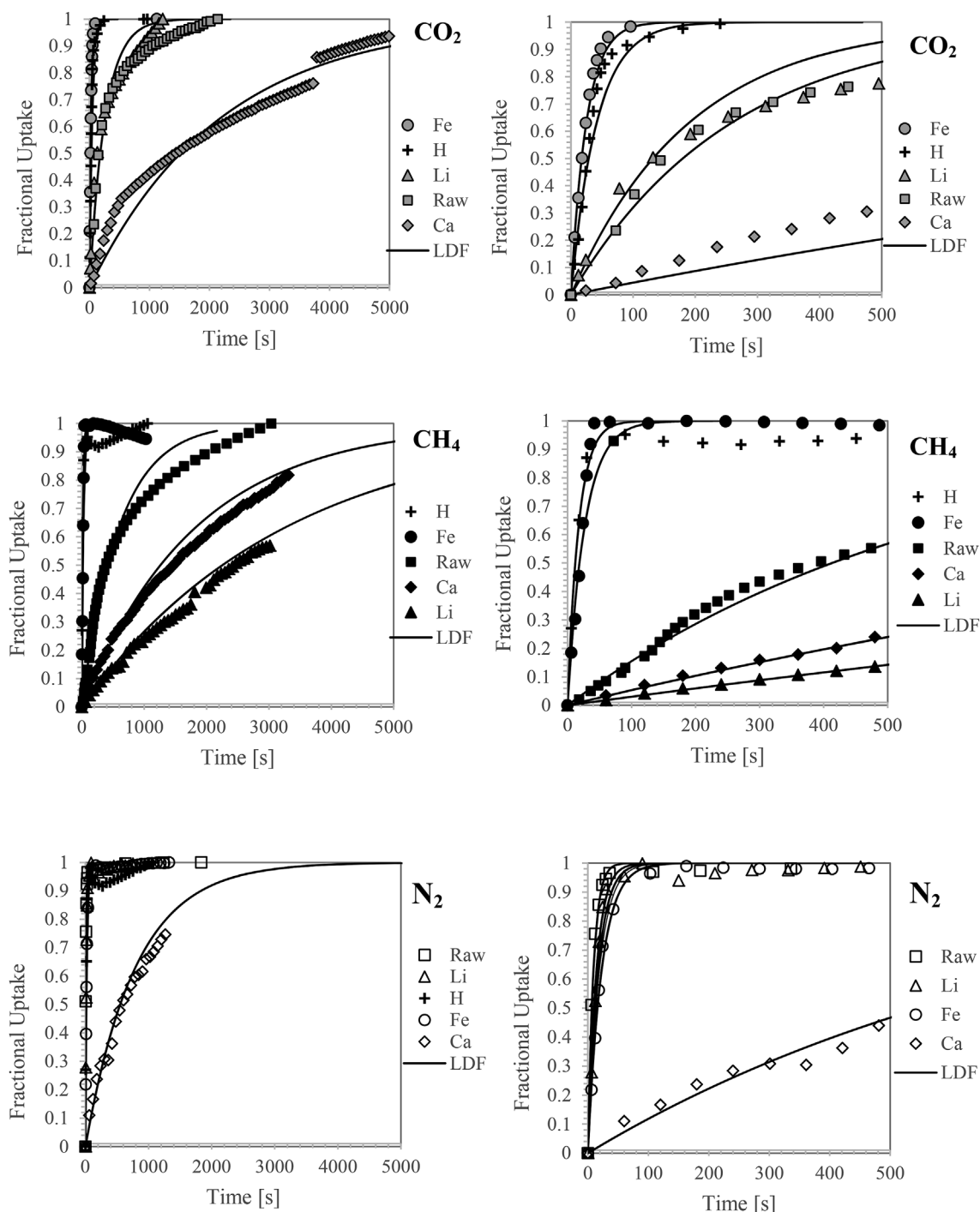
Fig. 9. Experimental adsorption fractional uptake rate curves and fitted LDF model for selected pure carbon dioxide (top), methane (middle), and nitrogen (bottom) adsorption on prepared clinoptilolite samples determined at 303 K with a pressure step change from 0.5 to 1 atm. The plots on the left are for the long time, the plots on the right are for the short time.

occurring cations in this study was $Ca^{2+} > K^+ > Mg^{2+} \gg > Na^{+\cdot}$. The results from this study suggest that the starting cation type, content, and distribution within the natural clinoptilolite plays an important role in determining the outcome of the adsorbent kinetic effects upon cation exchange.

6. Conclusions

The influence of acid treatment and cation exchange modifications of natural clinoptilolite using monovalent, bivalent, and trivalent cations was studied. The compositional and structural properties of the samples were assessed using EDS and XRD analysis. Cation exchange is

shown to slightly alter the structure of the clinoptilolite and/or the extra framework atomic positions within the unit cell, as quantified by small changes observed in peak intensity of the XRD diffractograms. This is particularly evident following the substitution of the more acidic cations H^+, Li^+, Be^{2+}, Mg^{2+}, and Fe^{3+}. Dealumination of the zeolite lattice and incorporation of Fe^{3+} into the framework structure is hypothesized based upon the high amount of Fe^{3+} exchanged and the higher Si/Al ratio of 5.85 compared to a value of 5.1 for the naturally occurring raw clinoptilolite.

The adsorption characteristics of pure CO_2, N_2, and CH_4 gases were measured for all of the clinoptilolite samples. Langmuir and Toth isotherms were fitted to the experimental adsorption equilibrium data and
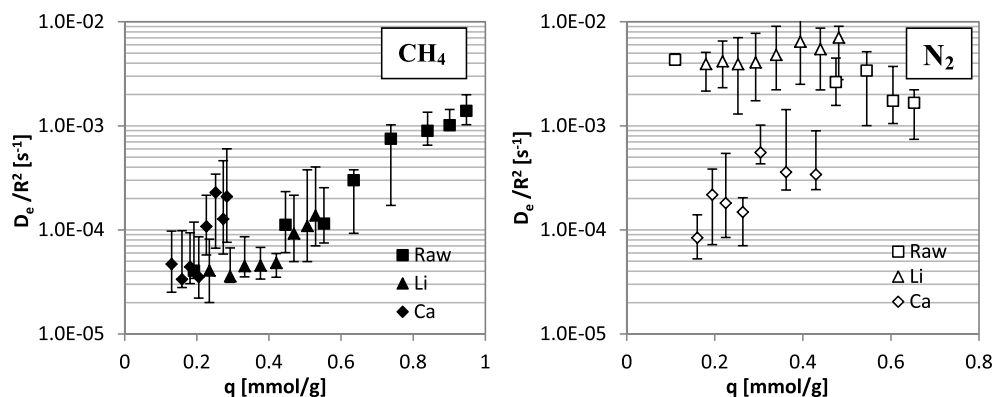
Fig. 10. Experimentally determined diffusion time constants as a function of total adsorbate concentration for pure nitrogen and methane on raw, Li^+, and Ca^{2+} clinoptilolite samples determined at 303 K.

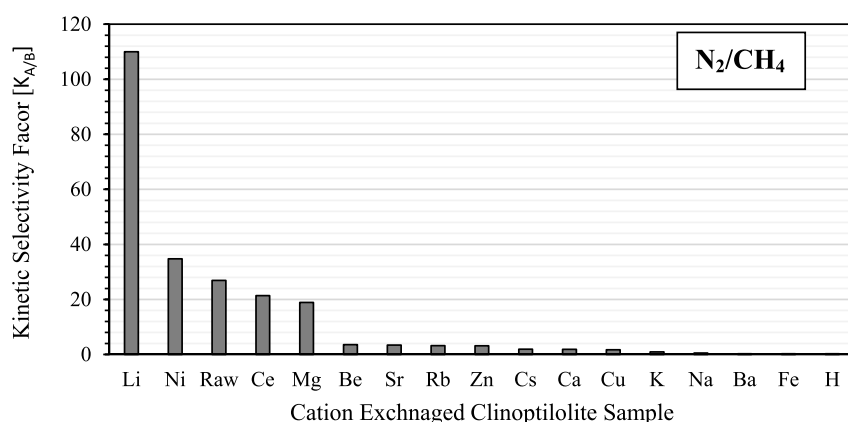**Fig. 11.** Experimentally determined kinetic selectivity factors for kinetic gas separations involving N_2-CH_4 with various prepared cation exchanged clinoptilolites at 303 K. The mass transfer coefficients obtained from the uptake data from a pressure step change of 0.5–1 atm was used.

the resultant parameters of these isotherms were determined. Diffusion time constants were assessed using the LDF approximation of the experimental gas uptake rate data. The positioning and type of charge balancing cations greatly influences the adsorption characteristics of the studied gases on the modified clinoptilolites compared to the original raw clinoptilolite. The results from this study establish that the starting cations found within the natural clinoptilolite influence the outcome of the adsorption equilibria and kinetic effects following cation exchange.

The adsorption equilibrium separation factor, and the kinetic selectivity factor were used for assessing the adsorbent performance for all of samples. This screening analysis shows that Cs^+ exchanged clinoptilolite has superior performance for possible CH_4/N_2 and CO_2/N_2 equilibrium separations. While the Ca^+ exchanged clinoptilolite exhibits promising equilibrium selectivity for CO_2/CH_4, this comes at the expense increased microporous diffusion resistance for both CO_2 and CH_4. Both Li^+ and Ni^{2+} clinoptilolites show favourable kinetic selectivity for possible N_2/CH_4 kinetic separations.

Appendix A. Supplementary data

Supplementary data related to this article can be found at http://dx.doi.org/10.1016/j.micromeso.2017.11.054.

Nomenclature

a,b,c	unit cell coordinate parameters [Å]
B	adsorption affinity constant [atm^{-1}]
D_e	effective (transport) diffusivity [m^2/s]
D_e/R_p^2	diffusion time constant [s^{-1}]
k_{LDF}	kinetic rate constant [s^{-1}]
$K_{A/B}$	kinetic selectivity [dimensionless]
n	dimensionless Toth model parameter [dimensionless]

P	pressure [atm]
q	adsorption capacity [mmol/g of adsorbent]
$q(t)$	amount absorbed at time t [mmol/g of adsorbent]
q_e	adsorption capacity at equilibrium [mmol/g of adsorbent]
q_m	adsorption capacity at saturation [mmol/g of adsorbent]
R_p	radius of particle [m]
t	time [s]
T	temperature [K]
S	adsorption equilibrium selectivity [dimensionless]
X	mole fraction in the gas phase [dimensionless]
Y	mole fraction in the gas phase [dimensionless]

Subscripts

A	component A
B	component B

Greek symbols

α	ideal adsorption equilibrium separation factor [dimensionless]
β	unit cell angle between a-c coordinates [°]
θ	adsorption surface coverage [dimensionless]

List of abbreviations

BDDT	Brunauer, Deming, Deming, and Teller
CMS	carbon molecular sieve
EDS	electron dispersive spectroscopy
HEU	heulandite
IZA	international zeolite association
MOF	metal organic framework
PSA	pressure swing adsorption
LDF	linear driving force
VSA	vacuum swing adsorption
XRD	x-ray diffraction

References

[1] D.D. Do, Adsorption Analysis: Equilibria and Kinetics, Imperial College Press, London, 1998.
[2] S. Sircar, Ind. Eng. Chem. Res. 45 (2006) 5435–5448.
[3] A.D. Buckingham, P.G. Hibbard, Symp. Faraday Soc. 2 (1968) 41.
[4] S. Cavenati, C.A. Grande, A.E. Rodrigues, Sep. Sci. Technol. 61 (2006) 3893–3906.
[5] S.M. Kuznicki, V.A. Bell, S. Nair, H.W. Hillhouse, R.M. Jacubinas, C.M. Braunbarth, B.H. Toby, M. Tsapatsis, Nature 412 (2001) 720–724.
[6] R.S. Pillai, S.A. Peter, R.V. Jasra, Microporous Mesoporous Mater 113 (2008) 268–276.
[7] R.P. Marathe, S. Farooq, M.P. Srinivasan, Langmuir 21 (2005) 4532–4546.
[8] N.K. Jensen, T.E. Rufford, G. Watson, D.K. Zhang, K.I. Chan, E.F. May, J. Chem. Eng. Data 57 (2012) 106–113.
[9] M.W. Ackley, R.F. Giese, R.T. Yang, Zeolites 12 (1992) 780–788.
[10] A. Jayaraman, A.J. Hernandez-Maldonado, R.T. Yang, D. Chinn, C.L. Munson, D.H. Mohr, Chem. Eng. Sci. 59 (2004) 2407–2417.
[11] M.W. Ackley, R.T. Yang, AIChE J. 37 (1991) 1645–1656.
[12] M.W. Ackley, R.T. Yang, Ind. Eng. Chem. Res. 30 (1991) 2523–2530.
[13] S. Cavenati, C.A. Grande, A.E. Rodrigues, J. Chem. Eng. Data 49 (2004) 1095–1101.
[14] V.P. Mulgundmath, F.H. Tezel, T. Saatcioglu, T.C. Golden, Can. J. Chem. Eng. 90 (2012) 730–738.
[15] D. Kennedy, F. Tezel, Adsorption 20 (2013) 189–199.
[16] P. Li, F. Tezel, J. Chem. Eng. Data 54 (2009) 8–15.
[17] P. Li, F.H. Tezel, J. Chem. Eng. Data 53 (2008) 2479–2487.
[18] V.P. Mulgundmath, F.H. Tezel, F. Hou, T.C. Golden, J. Porous Mater 19 (2011) 455–464.
[19] T.C. Golden, S. Sircar, J. Colloid Interface Sci. 162 (1994) 182–188.
[20] F. Dreisbach, R. Staudt, J.U. Keller, Adsorption 5 (1999) 215–227.
[21] S. Himeno, T. Komatsu, S. Fujita, J. Chem. Eng. Data 50 (2005) 369–376.
[22] J. Zhang, R. Singh, P.A. Webley, Microporous Mesoporous Mater 111 (2008) 478–487.
[23] T.E. Rufford, S. Smart, G.C.Y. Watson, B.F. Graham, J. Boxall, J.C. Diniz da Costa, E.F. May, J. Pet. Sci. Eng. 94–95 (2012) 123–154.
[24] M. Kacem, M. Pellerano, A. Delebarre, Fuel Process. Technol. 138 (2015) 271–283.
[25] A.I. Fatehi, K.F. Loughlin, M.M. Hassan, Gas. Sep. Purif. 9 (1995) 199–204.
[26] Y. Gogotsi, A. Nikitin, H. Ye, W. Zhou, J.E. Fischer, B. Yi, H.C. Foley, M.W. Barsoum, Nat. Mater 2 (2003) 591–594.
[27] A. Kapoor, R.T. Yang, Chem. Eng. Sci. 44 (1989) 1723–1733.
[28] S. Cavenati, C.A. Grande, A.E. Rodrigues, Adsorption 11 (2005) 549–554.
[29] J.W. Yoon, H. Chang, S.-J. Lee, Y.K. Hwang, D.-Y. Hong, S.K. Lee, J.S. Lee, S. Jang, T.U. Yoon, K. Kwac, Y. Jung, R.S. Pillai, F. Faucher, A. Vimont, M. Daturi, G. Férey, C. Serre, G. Maurin, Y.S. Bae, J.-S. Chang, Nat. Mater. 16 (2017) 526–531.
[30] M.M. Lozinska, E. Mangano, A.G. Greenaway, R. Fletcher, S.P. Thompson, C.A. Murray, S. Brandani, P.A. Wright, J. Phys. Chem. C 120 (2016) 19652–19662.
[31] M.A. Hernández, F. Rojas, V.H. Lara, J. Porous Mater 7 (2000) 443–454.
[32] N. Mansouri, N. Rikhtegar, H.A. Panahi, F. Atabi, B.K. Shahraki, Environ. Prot. Eng. 39 (2013).
[33] K. Koyama, Y. Takeuchi, Zeitschrift für krist, Cryst. Mater 145 (1977).
[34] Y. Garcia-Basabe, A. Gomez, I. Rodriguez-Iznaga, A. Montero, G. Vlaic, A. Lausi, A.R. Ruiz-Salvador, J. Phys. Chem. C 114 (2010) 5964–5974.
[35] J.R. Smyth, A.T. Spaid, D.L. Bish, Am. Mineral. 75 (1990).
[36] P. Yang, T. Armbruster, J. Solid State Chem. 123 (1996) 140–149.
[37] M.E. Gunter, T. Armbruster, T. Kohler, C.R. Knowles, Am. Mineral. 79 (1994).
[38] T. Armbruster, P. Simoncic, N. Döbelin, A. Malsy, P. Yang, Microporous Mesoporous Mater 57 (2003) 121–131.
[39] A. Sani, G. Vezzalini, P. Ciambelli, M.T. Rapacciuolo, Microporous Mesoporous Mater 31 (1999) 263–270.
[40] J. Stolz, P. Yang, T. Armbruster, Microporous Mesoporous Mater 37 (2000) 233–242.
[41] E.L. Uzunova, H. Mikosch, Microporous Mesoporous Mater 177 (2013) 113–119.
[42] A. Godelitsas, T. Armbruster, Microporous Mesoporous Mater 61 (2003) 3–24.
[43] Y. Garcia-Basabe, A.R. Ruiz-Salvador, G. Maurin, L.-C. de Menorval, I. Rodriguez-Iznaga, A. Gomez, Microporous Mesoporous Mater 155 (2012) 233–239.
[44] M.W. Ackley, R.F. Giese, R.T. Yang, Zeolites 12 (1992) 780–788.
[45] K. Koyama, Y. Takeuchi, Zeitschrift für krist, Cryst. Mater 145 (1977) 216–239.
[46] M. Johnson, D. O'Connor, P. Barnes, C.R.A. Catlow, S.L. Owens, G. Sankar, R. Bell, S.J. Teat, R. Stephenson, (2003).
[47] T. Armbruster, Am. Mineral. 78 (1993).
[48] L.T. Dimowa, O.E. Petrov, N.I. Djourelov, B.L. Shivachev, Clay Min. 50 (2015).
[49] M.W. Ackley, R.T. Yang, Ind. Eng. Chem. Res. 30 (1991) 2523–2530.
[50] A. Jayaraman, R.T. Yang, D. Chinn, C.L. Munson, Ind. Eng. Chem. Res. 44 (2005) 5184–5192.
[51] T.C. Frankwiwicz, R.G. Donnelly, Methane/nitrogen Gas Separation over the Zeolite Clinoptilolite by the Selective Adsorption of Nitrogen, American Chemical Society, 1983.
[52] R.W. Triebe, F.H. Tezel, Can. J. Chem. Eng. 73 (1995) 717–724.
[53] L. Predescu, F.H. Tezel, P. Stelmack, Stud. Surf. Sci. Catal. 97 (1995) 507–512.
[54] E. Kouvelos, K. Kesore, T. Steriotis, H. Grigoropoulou, D. Bouloubasi, N. Theophilou, S. Tzintzos, N. Kanelopoulos, Microporous Mesoporous Mater 99 (2007) 106–111.
[55] G. Aguilar-Armenta, G. Hernandez-Ramirez, E. Flores-Loyola, A. Ugarte-Castaneda, R. Silva-Gonzalez, C. Tabares-Munoz, A. Jimenez-Lopez, E. Rodriguez-Castellon, J. Phys. Chem. B 105 (2001) 1313–1319.
[56] A. Jayaraman, A.J. Hernandez-Maldonado, R.T. Yang, D. Chinn, C.L. Munson, D.H. Mohr, Chem. Eng. Sci. 59 (2004) 2407–2417.
[57] D.S. Karousos, A.A. Sapalidis, E.P. Kouvelos, G.E. Romanos, N.K. Kanellopoulos, Sep. Sci. Technol. 51 (2016) 83–95.
[58] B.E. Alver, M. Sakizci, Adsorption 21 (2015) 391–399.
[59] M.W. Ackley, R.T. Yang, Ind. Eng. Chem. Res. 30 (1991) 2523–2530.
[60] Structure Commission of the International Zeolite Association, M.M.J. Treacy, J.B. Higgins (Eds.), Collection of Simulated XRD Powder Patterns for Zeolites, Elsevier, New York, 2001.
[61] D.A. Kennedy, M. Mujcin, E. Trudeau, F.H. Tezel, J. Chem. Eng. Data 61 (2016) 3163–3176.
[62] S. Brandani, E. Mangano, L. Sarkisov, Adsorption 22 (2016) 261–276.
[63] S. Brunauer, L.S. Deming, W.E. Deming, E. Teller, J. Am. Chem. Soc. 62 (1940) 1723–1732.
[64] D.M. Ruthven, Principles of Adsorption and Adsorption Processes, John Wiley & Sons, 1984.
[65] I. Langmuir, J. Am. Chem. Soc. 40 (1918) 1361–1403.
[66] P.H. Nelson, S.M. Auerbach, J. Chem. Phys. 110 (1999) 9235.
[67] R. Yang, Gas Separation by Adsorption Processes, Butterworth Publishers, Toronto, 1987.
[68] S. Sircar, J.R. Hufton, Adsorption 6 (2000) 137–147.
[69] E. Glueckauf, Trans. Faraday Soc. 51 (1955) 1540.
[70] E. Glueckauf, J.I. Coates, J. Chem. Soc. (1947) 1315.
[71] C.R. Reid, K.M. Thomas, Langmuir 15 (1999) 3206–3218.
[72] D. Saha, Z. Bao, F. Jia, S. Deng, Environ. Sci. Technol. 44 (2010) 1820–1826.
[73] D.M. Ruthven, Chem. Ing. Tech. 83 (2011) 44–52.
[74] M. Çulfaz, M. Yağız, Sep. Purif. Technol. 37 (2004) 93–105.
[75] P. Castaldi, L. Santona, S. Enzo, P. Melis, J. Hazard. Mater 156 (2008) 428–434.
[76] F. Mumpton, Am. Mineral. 45 (1960) 351–369.
[77] W.S. Wise, W.J. Nokleberg, M. Kokinos, American Mineralogist 54 (1969) 887–895.
[78] R.A. Young, The Rietveld Method, Oxford University Press, 1993.
[79] A. Alberti, G. Vezzalini, TMPM Tschermaks Mineral. Und Petrogr. Mittl. 31 (1983) 259–270.
[80] L. Dimova, O. Petrov, M. Kadiyski, N. Lihareva, A. Stoyanova-Ivanova, V. Mikli, Clay Min. 46 (2011).
[81] A. Alberti, TMPM Tschermaks Mineral. Und Petrogr. Mittl. 22 (1975) 25–37.
[82] R.D. Shannon, IUCr, Acta Crystallogr. Sect. A 32 (1976) 751–767.
[83] J.C. Slater, J. Chem. Phys. 41 (1964) 3199–3204.
[84] S.-T. Yang, J. Kim, W.-S. Ahn, Microporous Mesoporous Mater 135 (2010) 90–94.
[85] K.S. Walton, M.B. Abney, M. Douglas LeVan, Microporous Mesoporous Mater 91 (2006) 78–84.
[86] A.O. Larsen, F.S. Nordrum, N. Dobelin, T. Armbruster, O.V. Petersen, M. Erambert, Eur. J. Mineral. 17 (2005).
[87] M. Sacerdoti, G. Lucchetti, Microporous Mesoporous Mater 131 (2010) 310–313.
[88] O. Cheung, N. Hedin, RSC Adv. 4 (2014) 14480–14494.
[89] K.T. Chue, J.N. Kim, Y.J. Yoo, S.H. Cho, R.T. Yang, Ind. Eng. Chem. Res. 34 (1995) 591–598.
[90] M. Mofarahi, F. Gholipour, Microporous Mesoporous Mater 200 (2014) 1–10.
[91] S. Oddy, J. Poupore, F.H. Tezel, Can. J. Chem. Eng. 91 (2013) 1031–1039.
[92] A. Arcoya, J.A. González, G. Llabre, X.L. Seoane, N. Travieso, Microporous Mater 7 (1996) 1–13.
[93] P.J. Harlick, F.H. Tezel, Sep. Purif. Technol. 33 (2003) 199–210.
[94] A. Bakhtyari, M. Mofarahi, J. Chem. Eng. Data 59 (2014) 626–639.
[95] R.J. Mohr, D. Vorkapic, M.B. Rao, S. Sircar, Adsorption 5 (1999) 145–158.
[96] Y.-J. Wu, Y. Yang, X.-M. Kong, P. Li, J.-G. Yu, A.M. Ribeiro, A.E. Rodrigues, J. Chem. Eng. Data 60 (2015) 2684–2693.
[97] X. Shao, Z. Feng, R. Xue, C. Ma, W. Wang, X. Peng, D. Cao, AIChE J. 57 (2011) 3042–3051.
[98] B. Yuan, X. Wu, Y. Chen, J. Huang, H. Luo, S. Deng, Environ. Sci. Technol. 47 (2013) 5474–5480.
[99] G. Narin, S. Yilmaz, S. Ulku, Chem. Eng. Commun. 191 (2004) 1525–1538.
[100] R.W. Triebe, F.H. Tezel, Gas. Sep. Purif. 9 (1995) 223–230.
[101] M.H. Chahbani, D. Tondeur, Sep. Purif. Technol. 20 (2000) 185–196.
[102] T.E. Rufford, G.C.Y. Watson, T.L. Saleman, P.S. Hofman, N.K. Jensen, E.F. May, (2013).